TOPICAL REVIEW

Single-photon generation and detection

To cite this article: G S Buller and R J Collins 2009 *Meas. Sci. Technol.* **21** 012002

View the article online for updates and enhancements.

ENABLING THE
TECHNOLOGIES
FOR SEMICON
It's Possible Sessions

November 30, 2021

PI
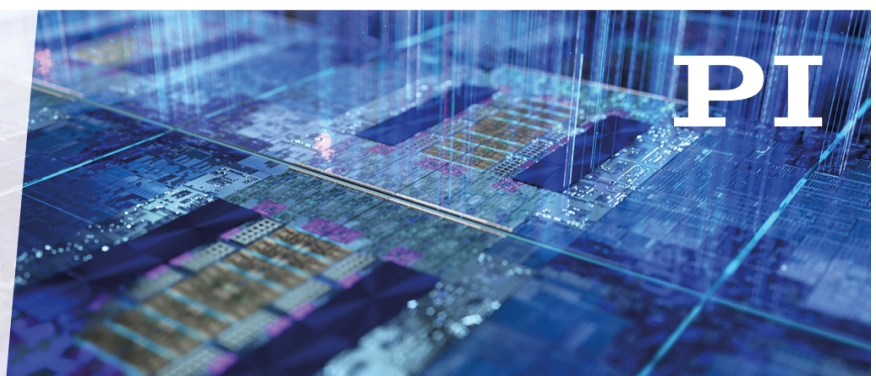
TOPICAL REVIEW

Single-photon generation and detection

G S Buller and R J Collins

School of Engineering and Physical Sciences, David Brewster Building, Heriot-Watt University,
Edinburgh, EH14 4AS, UK

E-mail: g.s.buller@hw.ac.uk

Abstract
The detection and generation of single photons has seen an upsurge in interest in recent years
as new scientific fields of research, for example quantum information processing, have been
established. This review serves to provide an overview of progress in these areas, describing
some of the main candidates for single-photon components for use in emerging fields of
research.

Keywords: single-photon sources, single-photon detection

1. Introduction

For many centuries, physicists have sought to understand the nature of light. From the early particulate theories, through wave models, to quantum theory, the understanding of light has been a vital area of scientific research. First proposed by Albert Einstein between 1905 and 1917, the photon is the elemental quantum of light [1, 2] (but also see [3] for additional important background). The fundamental boundaries on the precision with which certain properties of the single photon may be measured, as outlined by the Heisenberg Uncertainty Principle [4, 5], can be employed in several emerging fields of academic research. Methods of generation, detection and manipulation of single photons act as the enabling technologies which underpin several exciting new areas in optical physics. One such area is quantum cryptography, or more correctly quantum key distribution (QKD) [6], which is already on the fringes of commercial exploitation [7, 8], and offers the prospect of verifiably secure sharing of cryptographic keys by two or more parties, guaranteed by the laws of quantum mechanics. One of the propositions of quantum theory is wave–particle duality: a particle may behave as a wave or a particle but never both simultaneously. In Young's double-slit experiment [9] it is possible to either know the path the particle travelled through the equipment or to observe the wave-like interference fringes at the output [10], but not both. Any modification to the apparatus which allows the experimenter to know which slit the photon was transmitted through will prevent the interference pattern from being observed at the output. Demonstration of

the non-classical wave–particle duality requires that only one photon is present in the experimental apparatus at any given time and, therefore, is an ideal candidate for the application of single-photon sources [11]. The field of quantum computing relies on the processing of qubits, which are a superposition of two or more quantum states. Quantum computing has the potential to provide vastly increased processing capabilities for certain important algorithms when compared to today's serial, semiconductor-based computer processors [12, 13]. Photons are potential candidates to form qubits in these systems, and Knill *et al* [14] proposed quantum computing using only single-photon sources, linear optical elements and single-photon detectors.

Single-photon detection also has applications in many fields where very high sensitivity detection of light is necessary. For example, in biophotonics applications the photon emission rate is often low and the relative working time with samples frequently necessarily short so that reliable and efficient single-photon detectors are essential [15]. Time-resolved photoluminescence of semiconductor structures will also require the examination of very low photo-generated carrier densities which necessitates highly efficient, low-noise detectors [16]. In time-of-flight laser ranging, the aim is to measure the return time of laser pulses reflected from a target to determine range data. If the transmitted optical pulse energies can be reduced to energy levels which, on average, produce single-photon returns per optical pulse from a given target then the possibility of eye-safe and covert operation can be achieved utilizing time-correlated single-photon counting (TCSPC),
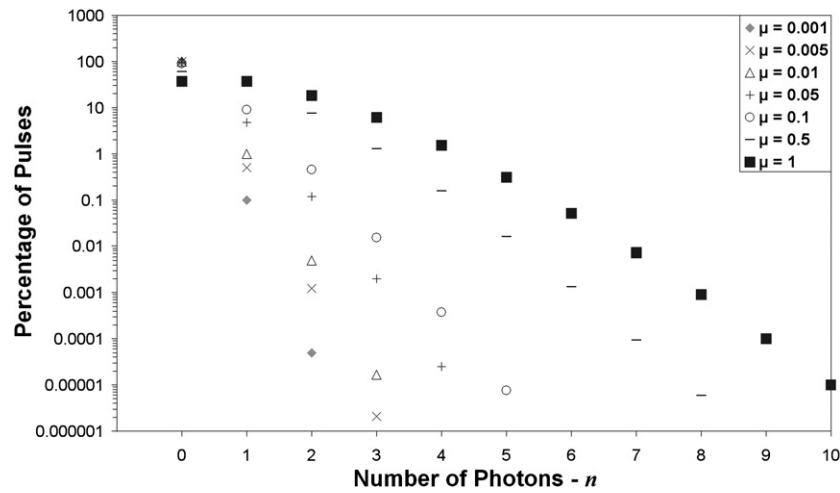
Figure 1. The number of photons in each pulse for a range of different average numbers of photons per pulse.

typically in conjunction with low-jitter single-photon counting detectors [17]. In all these applications, a form of TCSPC detection is being used and, in at least some of these cases, the current spectral detection boundaries are proving to be a restriction.

This review aims to act as an introduction to the topics of single-photon generation and detection for the general scientific reader and to provide a broad introduction to the current technologies available. We will examine key candidates for single-photon generation including colour centres in diamond and emitters based on semiconductor quantum dots. The single-photon detector technologies described will include the rapid advances in semiconductor avalanche diode detectors, especially into the near-infrared region, and the emergence of superconducting single-photon detectors which offer a much wider spectral range of operation than currently available from semiconductor-based single-photon detectors.

2. Single-photon generation

2.1. Weak coherent pulses

The generation of single photons on demand is currently less well developed than the detection of single photons. Consequently, many quantum key distribution experiments use pseudo-single-photon sources such as weak coherent pulses (see [18–23] for examples). Weak coherent pulses (WCP) are laser pulses that have been attenuated so that the mean number of photons per pulse (μ) is smaller than 1. WCP sources are not true single-photon sources; the number of photons in each pulse follows Poissonian statistics [21], that is to say the probability, $p(n, \mu)$ of a pulse attenuated to a particular value of μ containing n photons is given by [24]

$$p(n, \mu) = \frac{\mu^n \, \mathrm{e}^{-\mu}}{n!}. \qquad (1)$$

A plot of percentage of pulses against number of photons, such as that shown in figure 1, shows that for different values of μ there is a certain probability of each pulse containing more than

one photon or no photons. Deciding on a value for μ depends on the application and is a compromise between multi-photon pulses and empty pulses. A typical value for μ in quantum key distribution (QKD) experiments is 0.1 (see [18–23] for examples) although this is not necessarily the optimal value to ensure the maximum secure bit rate [19, 25].

Substituting $n = 0$ into equation (1) leads to the following formula for the probability of a pulse containing no photons (a vacuum pulse):

$$p(0, \mu) = \mathrm{e}^{-\mu} \qquad (2)$$

while substituting $n = 1$ leads to the following formula for the probability of a pulse containing only one photon:

$$p(1, \mu) = \mu \, \mathrm{e}^{-\mu}. \qquad (3)$$

From equations (2) and (3), we can derive the probability of a pulse that is not empty (non-vacuum, i.e. a pulse containing some number of photons greater than zero) containing more than one photon:

$$p(n > 1 | n > 0, \mu) = \frac{1 - p(0, \mu) - p(1, \mu)}{1 - p(0, \mu)}. \qquad (4)$$

On substituting in (3) and (4) we arrive at

$$p(n > 1 | n > 0, \mu) = \frac{1 - \mathrm{e}^{-\mu}(1 + \mu)}{1 - \mathrm{e}^{-\mu}} \qquad (5)$$

and this is plotted for a number of different values of μ in figure 2.

From figure 2 it can be seen that if $\mu = 0.1$, approximately 5% of the non-empty pulses contain more than one photon. Since a certain percentage of the pulses contain multiple photons an eavesdropper listening to the QKD transmission can potentially isolate a photon from each multi-photon pulse for analysis while allowing the remainder to continue to Bob [26]. In a multi-user QKD system (one Alice and multiple Bobs) there is an additional problem in that there is a possibility that two (or more) Bobs may share bits from the same key [20].
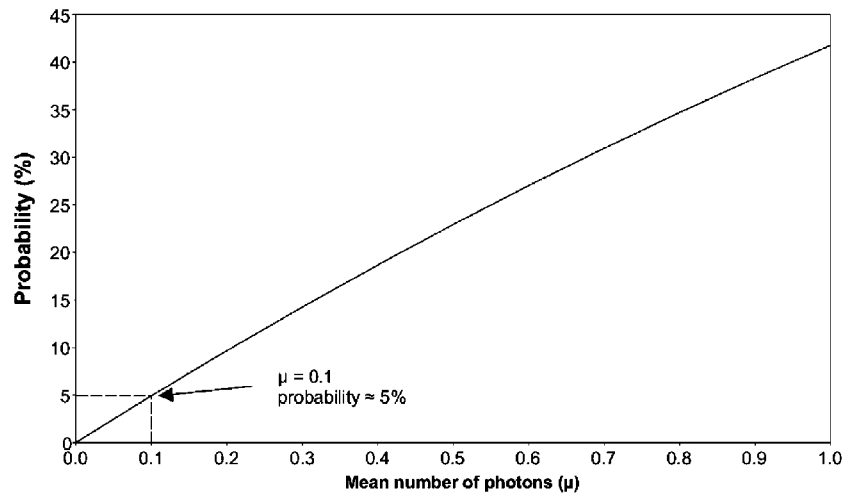
Figure 2. The probability of a non-empty pulse containing more than one photon for a number of different mean numbers of photons per pulse.
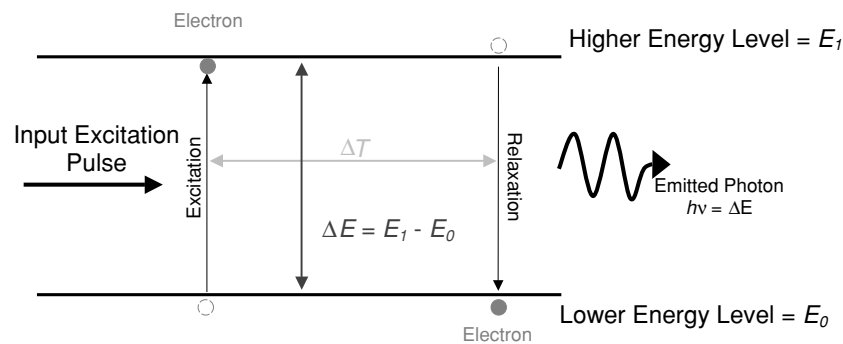
Figure 3. A model of a two-level atom. The electron is initially in the lower energy level (E_0) until it receives an input excitation pulse whereupon it is excited to the higher energy level (E_1). After a period of time ΔT has elapsed, the electron will relax back to the lower energy level, emitting a photon as it does so. The energy of the photon, measured as Planck's constant (h) multiplied by the frequency (ν) is equal to the difference between the two energy levels (ΔE).

2.2. Single hydrogen-like atom

Despite the obvious limitations of the WCP approach, for convenience they are used in many experimental implementations of QKD. The limitations mean that there has been interest in developing single-photon sources with lower vacuum and multi-photon rates. A conceptually simple single-photon source is the two level atom system, as covered in many textbooks (for example [27–29]) and shown in figure 3. In this case, the electron is excited to a higher energy level by an input energy pulse and then relaxes to a lower level by emitting a photon [1, 2, 29]. The wavelength of the emitted photon is dependent on the difference between the two energy levels and is given by

$$\lambda = \frac{hc}{\Delta E} = \frac{c}{\nu} \qquad (6)$$

where is h Planck's constant (6.62607×10^{-34} J s), c is the speed of light in a vacuum ($299\,792\,000$ m s^{-1}), ν is the frequency and ΔE is the difference in energy between the two levels.

An important issue with this approach to the generation of single photons lies in the isolating of a single atom. Atomic spacings are typically of the order of 0.1–0.5 nm [27].

The excitation of adjacent atoms may result in the emission of multi-photon pulses which may have disadvantages for particular applications. Single atoms may be isolated using high-finesse cavities [30, 31], off-resonance optical traps [32], magneto-optical traps [33, 34] and ion traps [35].

Placing the atom in an optical cavity formed by two highly reflective mirrors will change the energies available to the emitted photon. The most suitable mirrors are distributed Bragg reflectors (DBR); many pairs of alternating high and low index layers, each of thickness $\lambda/4$ leading to stack reflectivities of greater than 99% [36]. The top mirror is made fractionally less reflective than the bottom mirror to increase photon emission preferentially in the upward direction.

In 2000 Pinkse *et al* succeeded in trapping a single atom in an optical cavity [30]. In 2007, the same research group published work detailing a single-photon source consisting of a single rubidium-85 atom contained in an optical cavity [31]. For excitation pulses operating at a pulse repetition frequency of 100 kHz, the photon generation and detection probability (which also includes the detection efficiency of the APDs used to detect the photons) was 0.93%.

One measure of the quality of a single-photon source is the second-order autocorrelation function—a measure of the
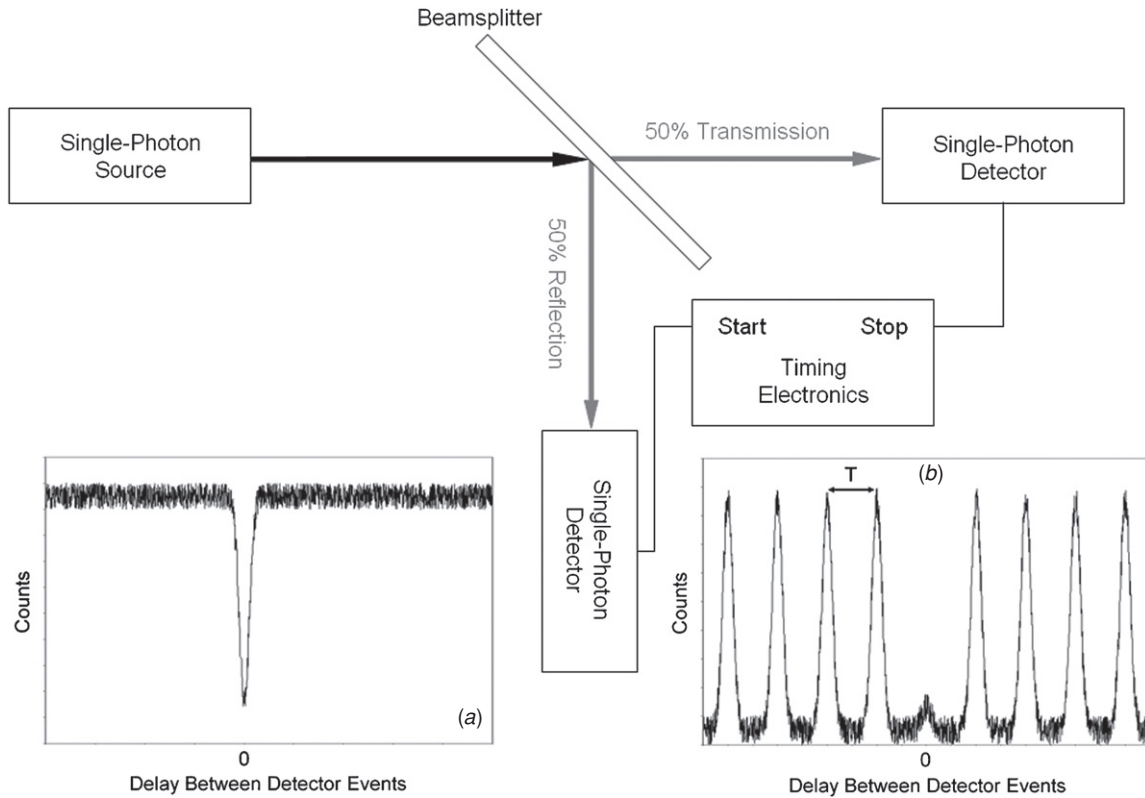
Figure 4. A schematic of a possible setup for Hanbury–Brown Twiss experiment. The optical output of the single-photon source is directed onto a 50% transmission/50% reflection beamsplitter. Two single-photon detectors are positioned to capture the two photon streams from the beam splitter. The system is arranged so that the total electrical and optical delay for both arms is exactly the same. If the timing electronics register an event from both detectors simultaneously, the source is emitting multi-photons as single photons cannot be split at a beamsplitter. Inset (a) shows a simulation of histogram which would be obtained for a good single-photon source which was illuminated using continuous wave (CW) light. There is a dip in the otherwise uniform count level at a time corresponding to both detectors firing simultaneously. Inset (b) shows a simulation of a histogram which would be obtained for a good single-photon source which was excited using pulsed excitation. There are a series of peaks which are spaced in time by T, the pulse repetition period of the excitation. The peak corresponding to both detectors firing simultaneously is highly suppressed.

number of multi-photon pulses in relation to single-photon pulses. The second-order autocorrelation function ($g^{(2)}(\tau)$) is defined as

$$g^{(2)}(\tau) = \frac{\langle n(t)n(t+\tau)\rangle}{\langle n\rangle^2} \qquad (7)$$

where $n(t)$ is the photocount probability at time t and the angular brackets denote ensemble averages. This can also be written in terms of the conditional probability of recording photodetections at times t and $t + \tau$ (which is denoted by $p(t : t + \tau)$), normalized by the probability of recording a single detector event (which is denoted by $p(t)$):

$$g^{(2)}(\tau) = \frac{p(t : t+\tau)}{p(t)}. \qquad (8)$$

Two detector events occurring simultaneously (i.e. at $\tau = 0$) will have been have produced by a multi-photon pulse. The closer to zero the value of $g^{(2)}(0)$, the greater the ratio of single photons to multi-photons in the optical emission.

The value of $g^{(2)}(0)$ can be measured using a Hanbury–Brown and Twiss experiment, as shown in figure 4 [37]. The output of the single-photon source is directed onto a 50% transmission, 50% reflection beamsplitter and the resulting two beams from the beamsplitter are directed onto respective

individual detectors through equal length paths. Clearly, if both detectors register a photo-generated event at the same time, the photons which created this situation must be coincident and the source is outputting multi-photons. For the 2007 results detailing a single rubidium atom in an optical cavity, the value of $g^{(2)}(0)$ was 0.054 and was entirely limited by dark counts and background illumination of the single atom.

In 2005, Darquié *et al* demonstrated a single rubidium-87 atom [38] trapped in a far-detuned optical trap. The single-photon source was operated at a repetition rate of 5 MHz. The photon generation and detection probability (which also includes the detection efficiency of the APDs used to detect the photons) was 0.60% ± 0.04%. The probability of single-photon emission was 98.1% and the probability of double-photon emission was 1.9% [38].

2.3. Colour centres in diamond

The technical challenges involved in using single atoms have led to research into other techniques to generate single photons. In 1957 Kaiser and Bond identified nitrogen as a common impurity in diamond [39]. It is possible to substitute a nitrogen atom for a vacancy in an adjacent lattice position to generate an

optically pumped source of single photons at room temperature [40, 41]. Both the ground and optically excited levels are triplet states and the photon emission is broadband ($\Delta\lambda \sim$ 100 nm) with wavelengths in the range 640–720 nm. Following this work, research has concentrated on identifying other potential impurities which may act as photon emitters, to the extent that over 500 optical centres have now been identified [42, 43]. Potential alternative optical centres include silicon [44] and nickel–nitrogen NE8 [45]. The high refractive index of diamond (2.4175 to 2.4178 [28]) means that the number of photons which can be collected from microscopy on a flat interface is greatly reduced due to total internal reflection. To overcome this problem, it is possible to use nanocrystals with size of the order of 50–100 nm, ensuring that no total internal reflection takes place [46].

Photonic emission from silicon vacancies in diamond was first demonstrated by Vavilov *et al* in 1980 [47] and verified by Clark *et al* in 1995 [48]. In 2005, Wang *et al* demonstrated a way to produce silicon vacancies in diamond by ion implantation [44], a technology which may be applied to the formation of any required impurities in diamond. This technique allows precise control over the location and density of the introduced impurities.

Nickel nitrogen NE8 defects in diamond have narrow spectral bandwidth ($\sim$1.5 nm) emissions around a wavelength of 800 nm [49]. These defects can be fabricated in thin diamond films by using chemical vapour deposition [50]. The first demonstration of stable, triggered, room temperature operation of a NE8 defect single-photon source was made by Wu *et al* in 2007 [45]. Under CW (continuous wave) excitation, this single-photon source demonstrated a $g^{(2)}(0)$ of 0.2 while under pulsed excitation the $g^{(2)}(0)$ was 0.16.

The current highest single-photon emission rate from a colour centre in diamond is 1.6 MHz (before correction for detector efficiency) at a wavelength of 734 nm [51]. These results were obtained using an unknown impurity in diamond crystals of up to 2 μm in size. A $g^{(2)}(0)$ of 0.16 was observed for this single-photon source.

In 2002, Beveratos *et al* demonstrated a quantum key distribution system using a nitrogen vacancy in diamond as a single-photon source [52]. This system achieved an average of 77 secure bits in a 10 ms operation window, leading to an approximate average secure key exchange rate of 7700 bit s^{-1} using a polarization-based BB84 protocol [52].

In common with single atoms, it is possible to couple the emission from colour centres in diamond into a cavity to improve the efficiency of the emission. In principle, it is possible to form the required cavity from the diamond itself [53, 54]. However, the first demonstrations exhibited high scattering losses as the diamond was composed of many crystalline structures (polycrystalline) [55, 56]. It is possible to use cavities formed from materials other than diamond, such as silica microspheres [57] but this technique has the potential disadvantage that it is often realized by the random deposition of diamond nanocrystals onto the surface of the microsphere. This can lead to large variations in the coupling between the diamond nanocrystal and the cavity.

In 2009, Barth *et al* demonstrated the controlled coupling of a single diamond nanocrystal to a polycrystalline cavity
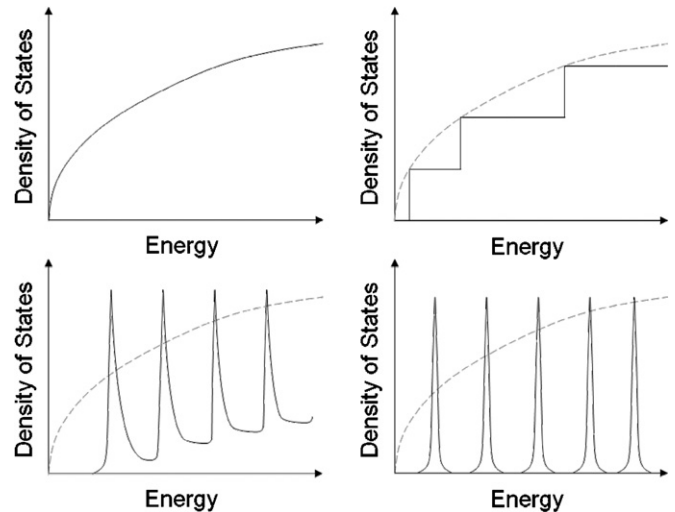
Figure 5. The density of states for (from left to right, top to bottom) a 3D bulk semiconductor, a 2D quantum well, a 1D quantum wire and a 0D quantum dot [24].

composed of silicon nitride (Si_3N_4) [58]. This work was preliminary to the application to a single-photon source and used nanocrystals containing many nitrogen vacancy photon emitters.

2.4. Quantum dots

The challenges involved in overcoming the practical difficulties in isolating single atoms make their use as single-photon sources very demanding. One alternative is to use larger structures which exhibit some of the characteristics of single atoms—in effect, artificial atoms. Such structures exist and are known as quantum dots. A quantum dot is a structure which confines electrons in three dimensions, leading to a quantization of the available energy transitions for carriers similar to that of a single atom. One common manifestation of a quantum dot is a nanometre dimensioned island of low band gap semiconductor material surrounded by higher band gap material (the band gap is a region of energies in which no electron states exist—an electron cannot take an energy level within the band gap) [59]. A quantum dot can exhibit single-photon emission if a single energy transition is selected [60–62]. A bulk semiconductor has a density of states, $g(E)$ (a measure of the number of energy states per unit volume which have an energy in the range E to $E + dE$), which is given by

$$g_{3D}(E) = \frac{m^*\sqrt{2m^*E}}{\pi^2\hbar^3} \qquad (9)$$

where E is the carrier energy, $\hbar = \frac{h}{2\pi}$, and m^* is the effective mass [63]. As shown in the top left-hand graph in figure 5 the density of states for a 3D bulk semiconductor increases gradually for an increase in energy.

Quantum theory tells us that an electron can behave as both a wave and a particle. It has a mass (9.10938×10^{-31} kg)

but also has an associated de Broglie wavelength. The de Broglie wavelength is defined by

$$\lambda_{\text{de Broglie}} = \frac{h}{mv}\sqrt{\left(1 - \frac{v^2}{c^2}\right)} \qquad (10)$$

where m is the mass, v is the object's velocity and c is the speed of light in a vacuum [64]. If a macroscopic bulk semiconductor is reshaped so that in one dimension the size is close to the de Broglie wavelength of an electron, a quantum well will be formed. This quantum well confines the electron in one dimension while permitting free motion in the remaining two dimensions, leading to a quantization of the energy levels. The quantization can also be observed in the density of states shown in the top right-hand graph in figure 5, which is now described as

$$g_{2D}(E) = \frac{Nm^*}{\pi\hbar^2} \qquad (11)$$

where N is the number of the well sub-band [65]. It is more normal to grow quantum wells by using a thin layer of low band gap semiconductor sandwiched between two layers of a larger band gap semiconductor. The low band gap semiconductor acts as the quantum well while the larger band gap materials provide the confinement [66].

If the previously bulk semiconductor is reshaped again so that the size is comparable to the de Broglie wavelength in two dimensions, a quantum wire can be formed. In a quantum wire the electrons are confined in two dimensions but free to move in the third. The density of states for this is also shown in figure 5 in the bottom left-hand graph. If the semiconductor is now shaped so that it is smaller than the de Broglie wavelength in all three dimensions, we have a quantum dot [67, 68].

The final graph in figure 5 shows the density of states for a quantum dot. A quantum dot confines the electrons in all three dimensions and this leads to a series of discrete Lorentzian shaped energies in the density of states. The wavefunctions of the electrons are fully constrained within the dot and the dot consequently behaves like a single atom, even though it is made up of many atoms.

Quantum dots can be fabricated using a number of different techniques, including colloidal synthesis [69], viral assembly [70], electrochemical processes [71] and self-assembly [72, 73]. By far the method which produces the best results is Stranski–Krastanow growth, otherwise known as self-assembly. Layers of different semiconductors (heterostructures) with the same crystal axes are grown using molecular beam epitaxy (MBE) or metallo-organic chemical vapour deposition (MOCVD) [74–76]. Self-assembly requires two successive layers of semiconductor, each with a slight mismatch in the lattice parameter, to be deposited on the sample semiconductor crystal surface. The slight mismatch in the lattice parameter leads to strain which, in turn, leads to the spontaneous formation of small islands in the semiconductor surface to relieve the strain, after a critical number of layers have been grown, as shown in figure 6. It is these nanometre sized islands that are the quantum dots. The process of island formation reduces the strain energy but increases the surface energy and the process of dot growth involves the formation of equilibrium between these two competing energies [77].
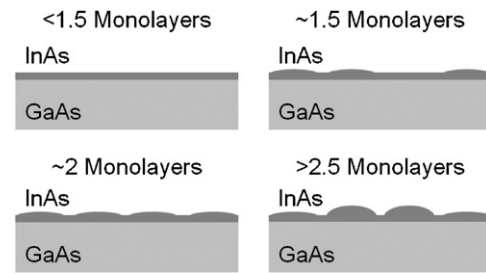
Figure 6. Stranski–Krastanow growth or self-assembly growth of InAs quantum dots on a GaAs substrate [72, 73]. At the critical thickness of 1.5 monolayers the lattice mismatch between InAs and GaAs results in the formation of small 'islands' to relieve the strain. Further layers increase the density until dislocations form at more than 2.5 layers when the dots begin to merge. After [59].
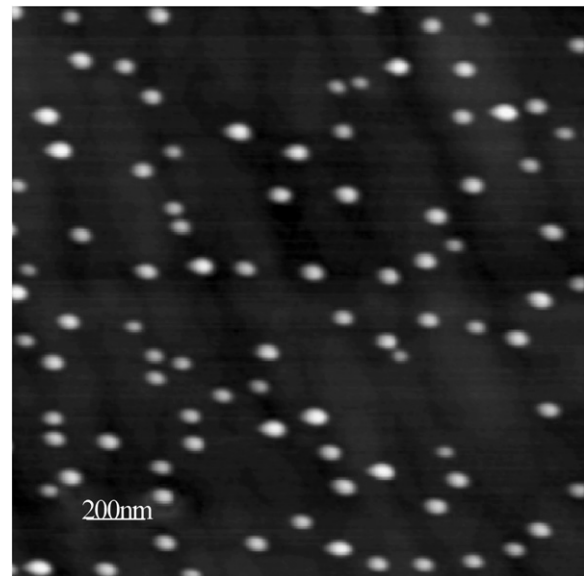
Figure 7. An atomic force microscopy (AFM) image of a quantum dot sample, similar to those which were further processed to create the micropillar samples examined in this thesis. The light spots are the small 'islands' of semiconductor which are the quantum dots and the inherently random placing of the dots can be clearly observed. Image courtesy of Engineering and Physical Sciences Research Council (EPSRC) National III–V Facility, University of Sheffield, UK.

Self-assembly produces dots which are well defined and of a high quality with no free surfaces and associated defects. MBE allows for some control over the density of dots on the sample surface as the source-sample geometry within the growth chamber can lead to a density gradient across the sample surface. Although semiconductor wafers are typically rotated during MBE growth to alleviate this density gradient, in the case of quantum dot growth such variations may be desirable and so the process of rotation can be reduced or stopped as required [78]. Dot densities of up to 10^{10} cm^{-2} are common [78]. Figure 7 shows an atomic force microscopy image of the surface of a quantum dot sample, where the light coloured spots are the quantum dots.

Due to the inherently random nature of the strain relief process, self-assembly does not allow any fine control over the positioning of the dots when using unpatterned semiconductor

substrates. While this may not be an issue for experiments conducted on large planar samples of quantum dots, in the case of microcavities there is a small probability that a microcavitiy will contain no quantum dots. Use of lithographic etching does allow the formation of regions in which dot formation is more favourable but the optical properties of such dots can be affected, as well as the samples requiring extensive preparation, somewhat reducing their usefulness [79].
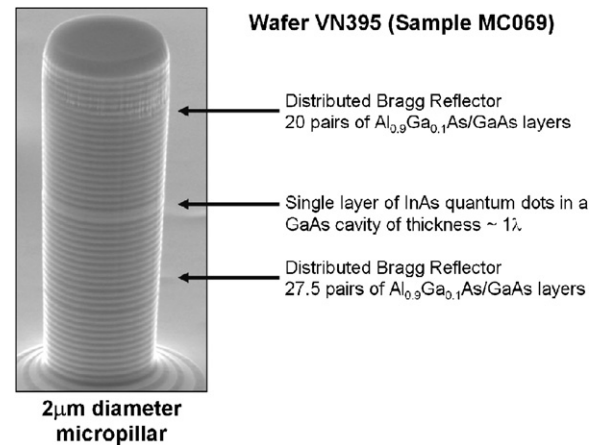
Quantum dots are good candidates for single-photon sources as they do not exhibit *photo-bleaching* (whereby the photon flux decreases with time [80]) or blinking (a discrete transition from an on, or high photon flux, state to an off, or low photon flux, state [81]). Generally, they must be operated at cryogenic temperatures to ensure that the carriers remain in the dot and the system is dominated by quantization. As the temperature is increased the occupation of the energy levels in the quantum dot changes and, at room temperature, there is a significant probability that carriers will leave the dot via vibrations in the atomic lattice. The excitation may be optical or electrical.

In 2000, Michler *et al* first demonstrated emission of light from a quantum dot with sub-Poissonian statistics—that is a photon number distribution with a variance less than the mean. These experiments demonstrated a $g^{(2)}(0)$ of 0.47 ± 0.02 using a cadmium selenide (CdSe) dot at room temperature [60]. This technique was refined with the introduction of spectral filtering to select a single energy transition (corresponding to a single emitted wavelength) by Santori *et al* giving a $g^{(2)}(0)$ of 0.12 (before subtraction of the background) [61].

Quantum dots emit photons isotropically so usually only a small fraction of the photons can be collected. Placing the quantum dot in a Fabry–Perot cavity, as shown in figure 8, will change the energies available to the emitted photon [62]. The thickness of the cavity will lead to the formation of a standing wave within the cavity, the cavity mode. At resonance, when the dot emits at the same wavelength as the cavity mode, the photon emission rate increases (leading to a decrease in the decay time, the Purcell effect [82]) and the photons are emitted into the cavity modes [59]. The Purcell effect provides an increase in the photon flux relative to an off-resonance dot and leads to a greater efficiency of single-photon generation. When a quantum dot is in resonance with the cavity, a decrease is observed in the lifetime of the dot emission. The associated Purcell factor is calculated by dividing the off-resonance decay time by the on-resonance decay time.

This resonance is a low temperature effect as at high temperatures the spectral full-width-at-half-maximum (FWHM) of the quantum dot emission is broadened and a matching cavity has a low quality factor and hence a low Purcell effect [59]. The wavelength of emission of a dot will increase with an increase of temperature, as will the wavelength of the cavity mode. However, the cavity mode will increase in wavelength at a lower rate so it is possible to temperature tune a particular dot into resonance with the cavity.

As the temperature of the quantum dot microcavity is increased, the spectral emission of the dot will broaden in linewidth and decrease in intensity. Consequently, it is not possible

Wafer VN395 (Sample MC069)

Distributed Bragg Reflector
20 pairs of Al$_{0.9}$Ga$_{0.1}$As/GaAs layers

Single layer of InAs quantum dots in a GaAs cavity of thickness ~ 1λ

Distributed Bragg Reflector
27.5 pairs of Al$_{0.9}$Ga$_{0.1}$As/GaAs layers

2μm diameter micropillar

Figure 8. A scanning electron microscope (SEM) image of a 2 μm diameter, 6 μm tall quantum dot pillar. The dot layer is clearly visible, as are the distributed Bragg reflectors (DBRs). The DBR consists of pairs of GaAs/AlGaAs layers and the top DBR has fewer layers to allow for the emission of photons. The top of the pillar shows a capping layer left over from the dot fabrication process which does not affect the dot emission characteristics. Image courtesy of Engineering and Physical Sciences Research Council (EPSRC) National III-V Facility, University of Sheffield, UK.

to increase the temperature of a quantum dot microcavity enough to bring every dot into resonance in turn; the emissions from some dots will have become too broad (and therefore, too low in intensity) before they are temperature tuned into resonance. The cavity mode is responsible for the majority of the multi-photon emissions in the narrow spectrum centred on the peak of dot emission. This means that a particular dot which is to be used as a single-photon source in resonance with a cavity must have a sufficiently high photon flux so that it dominates the multi-photon emissions from the cavity mode. To date, the highest on-demand single photon rate demonstrated from a quantum dot microcavity single-photon source is 31 MHz (after correction for the efficiency of the detectors) with a $g^{(2)}(0)$ of 0.4 [83].

In 2007, Intallura *et al* published details of a BB84 protocol, phase-based QKD system operating at a wavelength near 1.3 μm using a 1 MHz clock [84]. The microcavities were formed from a low-density layer of InAs quantum dots within a microcavity pillar of 3 μm diameter formed from 11 pairs of alternating AlGaAs/GaAs mirrors at the top and 30 pairs at the bottom. The optical excitation wavelength used was 1064 nm pumping at the clock frequency of 1 MHz. At the resonant temperature, the $g^{(2)}(0)$ of this single-photon source was 0.166.

Quantum dot microcavities may also be applied to a diode structure to create an electrically excited single-photon source [85]. Electrical excitation has the potential advantage over optical excitation that it is no longer necessary to isolate emitted photons from the excitation [86]. Such isolation (whether by spectral or spatial filtering) can introduce loss which reduces the flux of single photons available for use in applications. In 2009, Bimberg *et al* demonstrated a gigahertz clocked electrically excited quantum dot diode structure emitting photons of wavelength ~951 nm with a

$g^{(2)}(0)$ of 0, limited by the 0.7 ns timing resolution of the system, at a temperature of 15 K [86]. Diodes will be discussed in more detail in a later section. This device was formed from a 5×10^8 cm^{-2} density layer of InAs/GaAs quantum dots embedded in a p–i–n diode structure. The dot layer was confined between GaAs/AlGaAs distributed Bragg reflectors (5 on the top and 12 on bottom) forming a resonant cavity. A micron scale diameter aluminium oxide aperture inside the cavity above the dot layer allowed a single quantum dot to be electrically addressed. Such a device has potential applications in gigahertz clocked quantum key distribution over metropolitan access networks where the wavelength is suitably spectrally separated from the upstream and downstream classical communications [20].

2.5. Heralded photons

Perhaps one of the largest disadvantages of the single-photon sources described so far is that the emission is random. It is not possible to tell if a particular excitation pulse has generated a single-photon emission until that single photon is detected. It is possible to use parametric down-conversion to generate a 'heralded' source of single photons—'heralded' meaning that there is an indication of when a single photon was generated via detection of its pair photon [87, 88]. As shown in figure 9 a crystal with an optical nonlinearity (often of $\chi^{(2)}$ type) has a pump laser of a short wavelength (and therefore, high frequency) passed through it [88]. A beam dump is used at the far side of the crystal to block any pump laser photons which are transmitted through the crystal. The photon may occasionally annihilate to produce a photon pair at well-defined wavelengths with a total energy (measured as the sum of the frequencies) which is the same as the pump laser photons. These photons are emitted in a cone centred on the pump laser with one photon at a particular wavelength known as the 'signal' and the other the 'idler' [87, 88]. The relationship between the parameters of the signal, idler and pump photons is given by energy and momentum conservation and can be expressed as

$$E_S + E_I = E_P$$
$$\text{or} \quad \nu_S + \nu_I = \nu_P$$
$$\text{or} \quad \frac{1}{\lambda_S} + \frac{1}{\lambda_I} = \frac{1}{\lambda_P} \tag{12}$$

where E_S is the energy of the signal photon, E_I the energy of the idler photon and E_P the energy of the pump photon. Similarly, ν denotes frequency and λ wavelength. Since the signal and idler photons are generated as pairs, if spatial and spectral filtering is used on each of the two generated photon streams it is possible to use detection of one (say the 'idler') to confirm, or herald, the existence of the other (the 'signal') [87, 88].

This approach has been used on a number of occasions to generate heralded single photons for several different applications. In 2004, Fasel et al reported the generation of 1550 nm wavelength photons (with a 6.9 nm spectral width) heralded by 810 nm photons from a 532 nm wavelength pump source in a type I KNbO$_3$ bulk non-linear crystal [89]. The
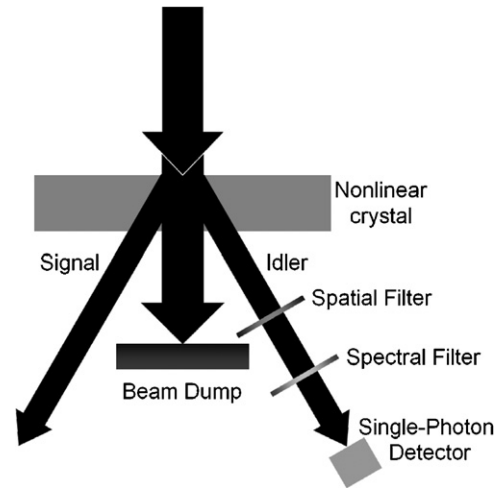
**Figure 9.** An example of a heralded photon source. After [88].

1550 nm wavelength photons were heralded with in excess of 60% probability and the probability of multi-photon emission was reduced by a factor of up to 500 when compared to Poissonian light. Castelletto et al reported the highly efficient generation of heralded single photons at a wavelength of 1550 nm and the collection of these into single spatial and spectral modes [90]. In 2007, Soujaeff et al published details of a heralded single-photon source producing signal photons at a wavelength of 1550 nm and herald photons at 521 nm [91]. At an input laser pulse repetition frequency of 82 MHz, the experiment produced single photons at a mean rate of 216 kHz.
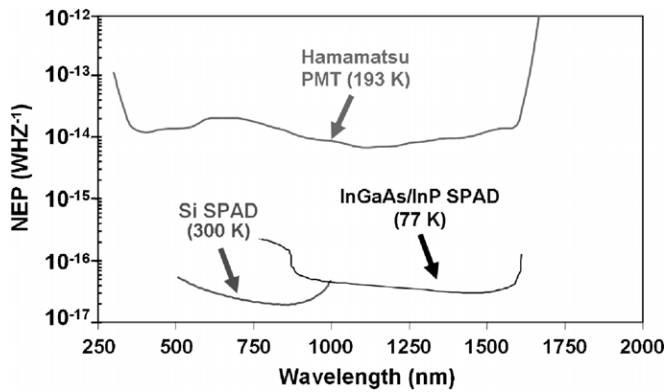
3. Single-photon detection

3.1. Characterization parameters

An important parameter in the choice of detector is the detection efficiency (η_D) which is the probability that an incident photon generates a measurable current pulse, assuming that the time between photon arrivals is greater than the dead-time of the detection system. The quantum efficiency (η_q) is the probability that an incident photon generates an electron–hole pair and is related to η_D by a factor which depends on the detector. Figure 10 shows a comparison of the detection efficiency spectra for three detectors of types which will be described in more detail later.

In photon-counting detectors, events will occur in the absence of incident radiation, or 'dark events'. The origin of these dark counts will vary depending on the detector types and operating conditions, for example in a photomultiplier thermionic emission at the photocathode will give rise to a quantifiable dark count rate. In photon-counting photomultipliers and avalanche photodiodes, the phenomenon of afterpulsing also occurs to form a contribution to the dark count rate. This happens when a detector event generated at a time t generates a subsequent event at a time $t + \Delta t$, where Δt is a largely unpredictable unique time difference for each photo-generated pulse. In addition there are further 'dark' (not generated by a photon) events, the exact cause of which
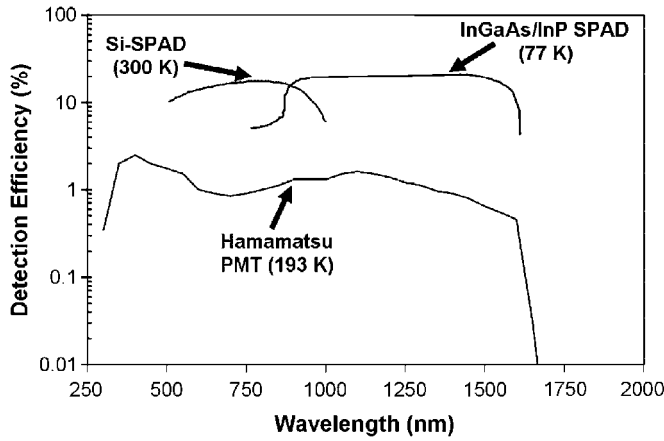
Figure 10. A comparison of the typical detection efficiencies of three different example detector technologies: a photo-multiplier tube (PMT) from Hamamatsu cooled to 193 K; an indium-gallium-arsenide/indium-phosphide (InGaAs/InP) single-photon avalanche diode (SPAD) cooled to 77 K [143] and a silicon (Si) SPAD at room temperature (300 K).

Figure 11. A comparison of the typical noise equivalent power (NEP) of three different detector technologies: a photo-multiplier tube (PMT) from, Hamamatsu cooled to 193 K; an indium gallium arsenide/indium-phosphide (InGaAs/InP) single-photon avalanche diode (SPAD) cooled to 77 K [143] and a silicon (Si) SPAD at room temperature (300 K).

depends on the configuration of the detector used but are often triggered by thermal excitation.

In many single-photon experiments, there are advantages in maintaining a low dark count rate as non-photon generated events will contribute to the overall error rate in measurements. A useful quantity in the characterization of single-photon detectors is the noise equivalent power (NEP), which is defined as

$$\text{NEP} = \frac{hc}{\lambda \eta_q} \sqrt{2N_D} \tag{13}$$

where λ is the wavelength of the incident photon, N_D is the dark count rate and η_q is the quantum efficiency, as defined before. The NEP is defined as the signal power required to attain a unity signal-to-noise ratio within a one second integration time [92] and is shown in figure 11 for the same three detectors presented in figure 10.

For many applications, the timing jitter of the detector is an important characterization parameter. The timing jitter
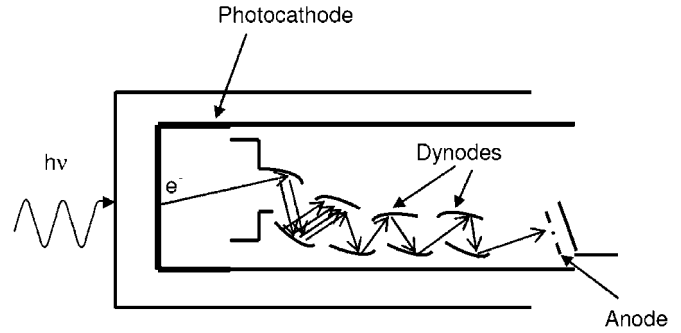
Figure 12. Schematic of a 'focused dynode chain' photomultiplier tube (PMT); the process of electron multiplication from each dynode stage causes a measurable current to be detected [72].

is a measure of the degree of variation in the delay between the arrival time of a photon at the detector and the output of an electrical pulse. It is common to take many different measurements of this delay and plot them in a histogram. The timing jitter is then quoted as being the full-width at half-maximum of the peak in this histogram. In time-of-flight laser-ranging, the timing jitter of the detector will affect the depth resolution of the measurement [93] while in QKD, the timing jitter can lead to intersymbol interference and increase the error rate of the key exchange process [94].

3.2. Photomultiplier tubes

Figure 12 shows a representational diagram of the operation of possibly the earliest form of single-photon detector to be used in a wide-range of applications; the photomultiplier tube (PMT) [95–98]. The device is formed from a vacuum tube with a photocathode at the entrance and a series of following dynodes arranged prior to an anode at the far end. The photocathode absorbs the incident photons and emits up to one electron per incident photon as it does so. Depending on the material composition of the photocathode, PMTs can be effective for detection of light at varying wavelengths. Generally, the photocathode consists of a thin evaporated layer of alkali metal compounds and one or more group V elements. Once an electron is emitted from the photocathode, it is accelerated towards, and collides with, the first positively charged dynode. This collision releases further electrons which are then accelerated towards the second dynode. Each successive dynode in the PMT is charged to a higher positive potential than the preceding one resulting in amplification as the increasing number of electrons collide with later dynodes. When compared to the semiconductor detectors which will be described later, PMTs have a high internal gain. If N dynodes are used, each with secondary electron coefficient α, then the multiplication factor, M, is given by

$$M = \alpha^N \tag{14}$$

Typical values of $\alpha = 4$ and $N = 10$ lead to a multiplication factor of 10^6 [99]. Typically, PMTs have multiplication factors which lie in the range 10^4–10^7.

When compared to the smaller active areas of semiconductor single-photon detectors, the large
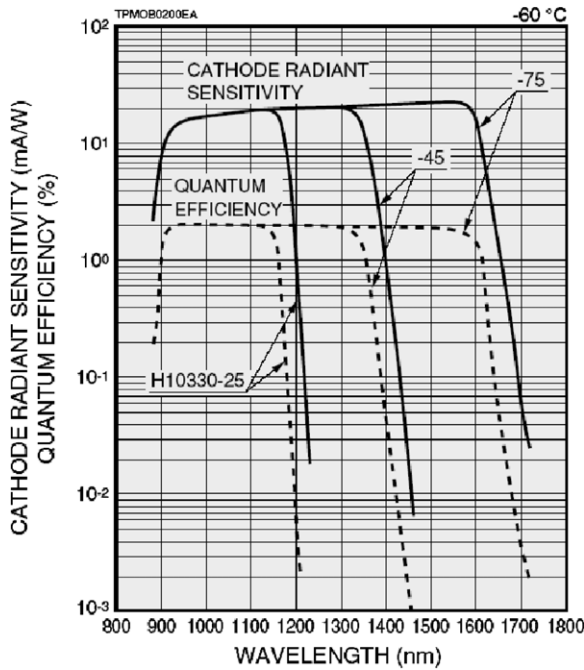
Figure 13. Quantum efficiency of three Hamamatsu PMT devices at −60 °C [75].

photocathodes used in PMTs (which can be up to 1000 times larger) are an advantage—facilitating improved optical collection, especially from extended optical sources [100]. However, the requirement to have several dynodes means that PMTs are contained in relatively large physical packages (although there have been advances in miniaturization [100]), have a poor mechanical stability and require high bias voltages, typically of the order of 1 kV. Although the single-photon detection efficiencies of PMTs are generally not greatly dependent on the wavelength of the incident photons, they typically exhibit low single-photon detection efficiencies [101, 102] and their timing jitter (which is mainly dependent on the fluctuations in transit times from the photocathode to the anode) is typically in the region of 1 ns [103]. The combination of these factors means that in applications where higher detection efficiencies and lower jitter are required, such as time-of-flight laser ranging [93, 104], PMTs are less likely to be used. The afterpulsing in PMTs is most likely caused by ion feedback or by luminescence of the dynode material and the glass of the tube while the dark counts are typically induced by thermal excitation [80].

If the photocathode is fabricated from InGaAs, and the device cooled to 200 K, it is possible to extend the spectrum of operation for a PMT into the near-infrared wavelengths up to 1700 nm [105]. The cooling is required to reduce the dark count rate which is typically around 10^5 counts per second at this temperature. Figure 13 shows the quantum efficiency of three devices manufactured by Hamamatsu; at best their efficiency is ∼2%. The cathode radiant sensitivity curve shows the ratio of the current transmitted by the photocathode to the incident radiant power of a specific wavelength. The quantum
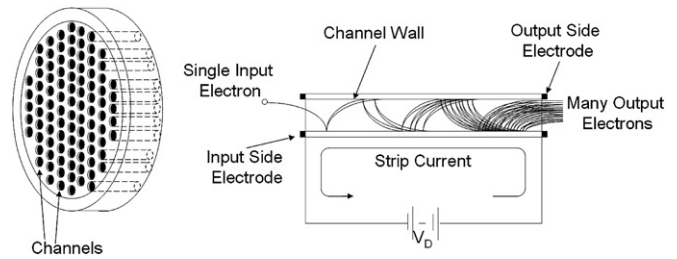
Figure 14. Micro-channel-plate (MCP) schematic and operating mechanism [106].

efficiencies of the three detectors follow different gradients as they are related by

$$\eta_q = S\frac{h\nu}{e} \qquad (15)$$

where S is the cathode radiant sensitivity, ν is the frequency of the light incident upon the detector and e is charge on an electron.

3.3. Microchannel plates

It is possible to consider microchannel plates (MCP) as an array of devices which operate along principles similar to those employed in the PMT. A schematic of the structure of a typical MCP is shown in figure 14, along with the method of operation. An MCP is assembled from an array of multiple ∼10 μm diameter thin glass capillaries arranged into a disc. Unlike in the case of the PMT, where there were separate dynodes positioned along the length of the tube, in an MCP the inner wall of each capillary is coated with a photo-emissive material and biased at each end, so that it acts as a continuous dynode [106]. The single input electron is accelerated by the positive potential towards the inner wall of the channel where it collides, releasing secondary electrons which then initiate further collisions along the length of the channel resulting in an exponential multiplication of the electron flux. MCP detectors require a high voltage of the order of 1 to 3 kV to operate but do not show the same multiplication factors as PMT detectors. Experiments by Becker indicated that some MCP devices do not exhibit any afterpulsing effects at timescales of up to 150 ns [80]. Typically, MCPs will exhibit timing jitters of approximately 20 to 30 ps [107].

The large 2D arrayed input means that the MCPs are good candidates to be used as detectors in imaging systems such as image intensifiers or time-of-flight laser-ranging systems [108].

3.4. Avalanche photodiodes

During the last 30 or so years, more rugged and efficient alternatives to dynode-based detectors have become more widely used: semiconductor detectors known as avalanche photodiodes. A diode is a device formed by a junction between a semiconductor with an excess of holes (p-type) and a semiconductor with an excess of carriers (n-type). These n-type and p-type regions are formed by the introduction of immobile dopant centres of opposite polarity within
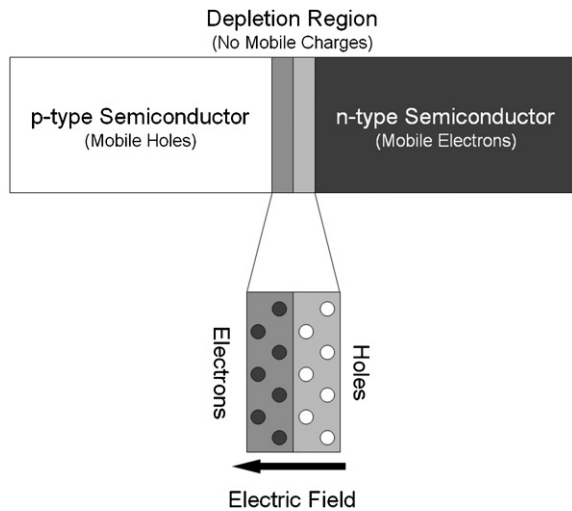
Figure 15. A schematic diagram of the structure of a diode. At the junction between the n-type and p-type semiconductor the mobile charges diffuse and create an electric field which prevents further charge diffusion. After [27].
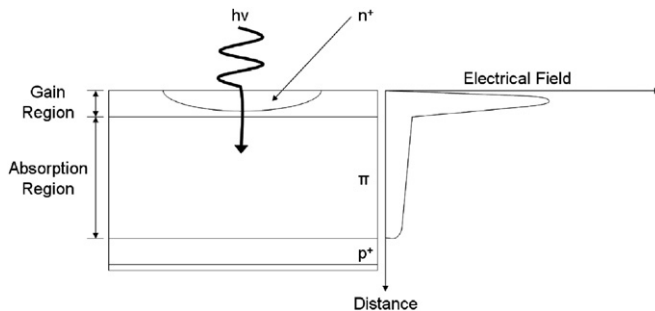
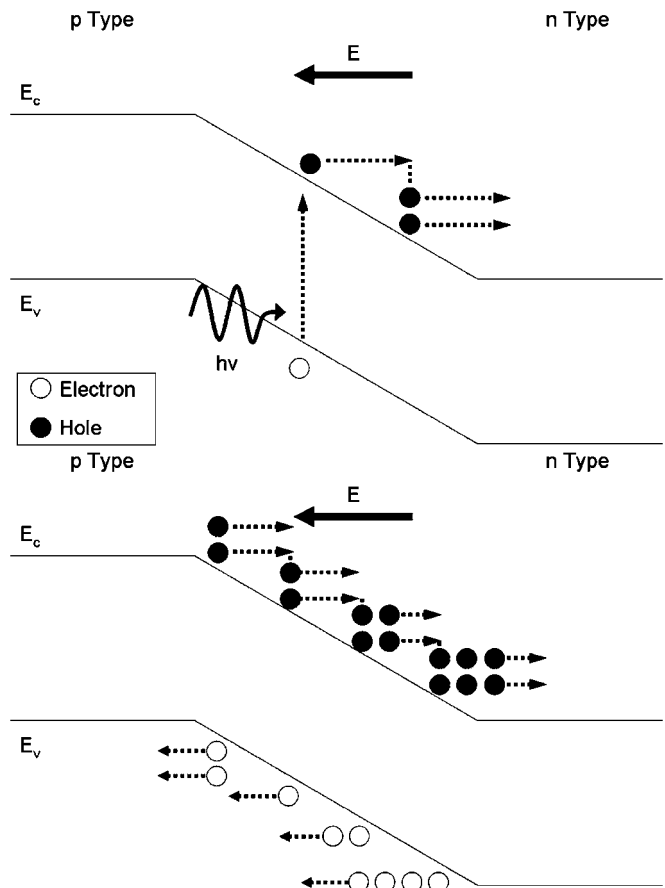**Figure 16.** The typical structure of a reach through avalanche photodiode (APD) is shown on the left while the right shows the electrical field within the device. After [100].


Figure 17. The process of impact ionization in an avalanche photodiode (APD). In the top schematic an electron–hole pair is generated by the absorption of a photon in the depletion region of a reverse biased APD—a process known as impact ionization. In the lower schematic the electron causes further impact ionizations, multiplying the number of electron–hole pairs and producing a self-sustaining avalanche of carriers.

the material. Because of the diffusion of carriers set up by the discontinuity between the two differently doped semiconductors, a region of electric field is formed which is depleted of all free carriers (as shown in figure 15) [100]. When a voltage is applied so that the n-type semiconductor is at a higher potential than the p-type, the junction is said to be reverse biased. When the electric field is sufficiently high, then a drifting electron can gain enough kinetic energy that, on collision with an atom in the lattice, it can knock an electron out of its bound state and promote it into the conduction band, releasing a hole in the valence band. This phenomenon is known as impact ionization, and a similar effect is seen for holes drifting in an electric field. These resulting carriers will then be accelerated in the high electric field and may undergo further impact ionization events, resulting in an avalanche of carriers—hence the term avalanche photodiode or APD.

Figure 16 shows a schematic of an example of a silicon reach-through avalanche photodiode and the corresponding electric field. The absorption region (in which the energy of the photon is absorbed) is produced from a thick layer of an undoped or lightly doped (intrinsic) semiconductor which is introduced between the p and n layers. This thick layer is introduced to ensure a high level of absorptance

of incident photons within the depleted region, as well as ensuring predominantly electron injection into the high-field multiplication region, the electron impact ionization coefficient in silicon being higher than the hole impact ionization coefficient. The use of this thick layer also helps reduce the capacitance of the device. In the gain region (also known as the multiplication region) the injected electron drifts from the point of absorption and undergoes impact ionization, initiating the avalanche process. This secondary electron–hole pair can lead to further impact ionization which will generate another electron–hole pair in a continuing process, as shown in figure 17 [100].

If the electric field applied across the device is sufficiently high to be above the avalanche breakdown threshold, it is possible for a single photo-generated carrier to induce a self-sustaining avalanche where the positive feedback from hole and electron impact ionization means that the avalanche process cannot stop. The point at which this occurs can be easily seen from the current–voltage characteristics of the device, as shown in figure 18. As the reverse bias voltage is increased, the current increases steadily until the voltage reaches the breakdown voltage where the current increases
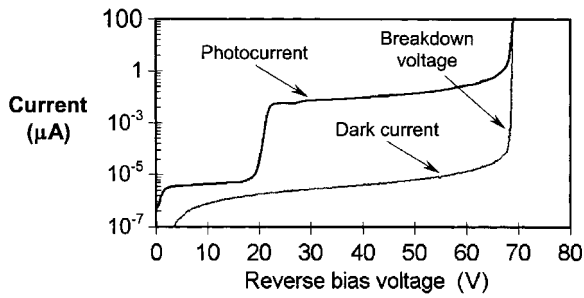
Figure 18. An example graph showing the change in photocurrent and dark current of an avalanche photodiode (APD) as the reverse bias voltage is increased towards breakdown voltage. This graph is for an InGaAs device manufactured by Fujitsu for use at a wavelength of 1300 nm.

rapidly, indicating that the carriers are beginning to multiply; however, at such a bias level the photocurrent will be linearly proportional to the incident light level. Above avalanche breakdown, a single electron (or hole) can initiate a self-sustaining current, the onset of which will be readily detectable by external thresholding circuitry. Such a mode of operation can be regarded as purely digital: the output is the same whether one or more photons are incident at the same time, quite different to the linear multiplication region of operation. When operated in this photon-counting, or Geiger, mode, the device is termed a single-photon avalanche diode or SPAD [109]. In order to stop the self-sustaining avalanche, it is necessary to reset the detector so that it is ready to receive more photons, i.e. the process of 'quenching' the avalanche.

The single-photon detection efficiency increases with the increasing excess bias voltage above avalanche breakdown primarily due the increase in the avalanche triggering probability, and possibly also due to the increase in the thickness of the depletion region [110]. The dark count rate also increases with increasing excess bias voltage due to the increase of both the avalanche triggering probability and the field-enhanced dark count generation [111, 112]. The rate of increase of dark count rate is usually greater than the rate of increase in photon detection efficiency. In addition, as the excess bias voltage is increased, the FWHM timing jitter decreases [109]. Consequently, the choice of optimal excess bias depends on the application to which the detector is applied. If the contribution of counts from other light sources is likely to greatly exceed the dark count rate (such as the solar background in the time-of-flight ranging application) then it may be preferable to increase the photon detection efficiency at the cost of increasing the dark count rate. In the case of quantum key distribution, measurements over long distances (i.e. high transmission channel losses) will be dominated by the dark count rate and increased timing jitter can lead to intersymbol interference. It is therefore necessary to balance the choice of excess bias to ensure sufficient detection efficiency, low timing jitter in comparison to the clock period and a low dark count rate.

3.4.1. Quenching. The process of quenching involves detecting the leading edge of the avalanche current, then generating a closely time-correlated electrical pulse, reducing
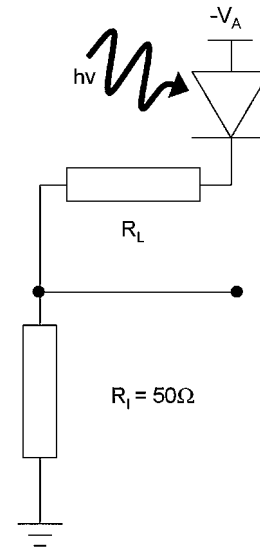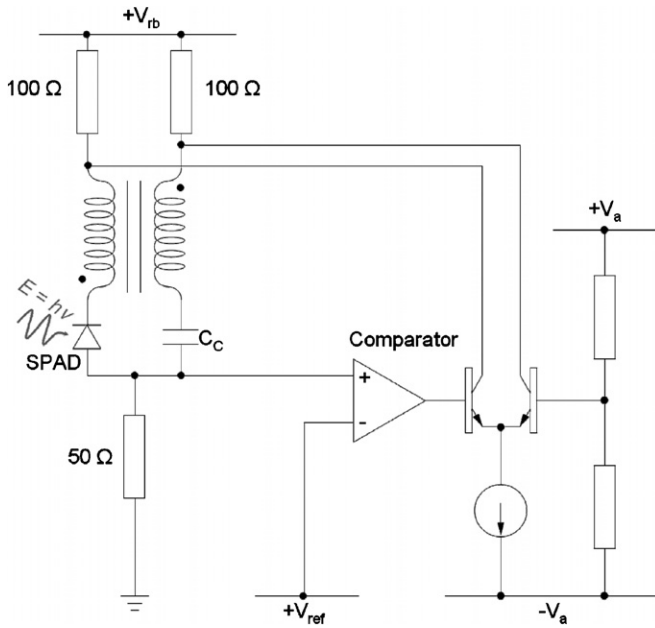

Figure 19. An example of a circuit used in passive quenching. When the avalanche photodiode (APD) is biased above the breakdown voltage by V_A an electron–hole pair can generate a self-sustaining avalanche. The avalanche discharges through the high resistance of R_L and the voltage V_A decreases. This is sensed by a comparator which produces a signal for photon counting and timing [113].

the bias voltage below breakdown level and finally restoring the voltage to the original operating level. There are three main forms of quenching applied to detectors: passive, active and gated.

A passive quenching circuit is simply a high impedance load connected in series to the SPAD [109, 113]. As shown in figure 19, the SPAD is reverse biased through a high ballast resistor R_L, of the order of kΩ. During a self-sustaining avalanche, the resistance of the SPAD drops to a few kΩ and the most of the external bias is dropped across R_1. Passive quenching circuits can have a slow recovery time in which no further photon detection events can be registered (a deadtime), reducing the maximum count rate possible. The recovery time depends on the product of the resistor R_L and the internal capacitance of the diode. Although it is possible to reduce both values to minimize the recovery time, even at small values of R_L ($\sim$500 kΩ) and internal capacitance ($\sim$1 pF), the recovery time can be up to $\sim$1 μs [109].

Active quenching was first developed by a group at Politecnico di Milano [114] and the basic circuit is shown figure 20 [115]. The photodiode is biased from the low impedance (100 Ω) source. The avalanche current induced by a photon event triggers a fast comparator which switches the current in an emitter-coupled transistor pair. A negative pulse is then superimposed on the bias and rapidly quenches the avalanche. Due to the additional propagation delays caused by the path through the comparator, the emitter-coupled transistor pair and the leads of the feedback loop, the leading edge of this pulse is delayed with respect to the onset of the avalanche and the duration of the avalanche current pulse is set by this delay. The hold-off time after quenching is determined by the duration of the comparator output pulse and is equal to that of the avalanche pulse. The deadtime associated with this

Figure 20. An example of a circuit used to perform active quenching [115].

technique is the sum of the avalanche and hold-off durations (approximately twice the duration of the propagation delay in the feedback loop) and can be of the order of a few nanoseconds—permitting photon detection rates of the order of Mbit s^{-1}.

It is important to note that the quenching voltage pulse induces a capacitive current flow in the diode which can be comparable to the avalanche current. This means that the comparator would be retriggered on the trailing edge of the pulse and the circuit would begin to oscillate. To alleviate this, the capacitive current peak is cancelled by a current pulse which has the same shape but opposite polarity, obtained by coupling the complementary output to the comparator unit via an adjustable compensating capacitor (C_C in figure 20). A transformer is used to equalize the shapes of the complementary pulses. This results in a slightly increased deadtime due to the degradation of the trailing edge of the pulse at the comparator input and the increased delay of the feedback loop.

In gated quenching, the bias voltage is only increased above the breakdown level for the duration of the period in

which a photon is expected. A form of gated quenching is used for most InGaAs/InP SPADs. This approach is applicable to QKD as the arrival times of the photons at the detectors, corresponding to the individual binary digits (bits) sent by Alice, can be predicted with reasonably high accuracy. However, in other applications such as time-of-flight-ranging, this technique is less appropriate since the arrival time of the photons at the detector is dependent on the unknown distance to the target.

3.4.2. Silicon single-photon avalanche diodes. Silicon single-photon avalanche diode detectors have been used for several decades [114, 115], and have become widely used in a number of photon-counting application areas in the spectral region 400–1000 nm.

There are two main types of design of Si-SPAD architecture: thick and thin junction. Both thick [116] and thin [117] junction Si-SPADs are now commercially available technologies. As may be guessed from the different terms, the main difference between the two designs is the thickness of the depleted region in which photon absorption takes place (see figure 21) [118]. In the case of a thick junction SPAD [119] this can be a few tens of μm whereas in the case of the thin junction it is typically only a few μm [118].

Generally, the thin-junction devices have lower single-photon detection efficiency (SPDE) than the thick junction, and the long interaction length of the latter leads to improved efficiency in the near-infrared. Figure 23 shows a comparison between the detection efficiencies of typical thick and thin junction Si-SPADs [109]. It can be seen from figure 22 that a typical thin junction Si-SPAD has a peak detection efficiency of ~52% at a wavelength of ~525 nm, falling to ~3% at a wavelength of 1000 nm. A typical thick junction Si-SPAD has a peak detection efficiency of ~70% at a wavelength of ~800 nm, falling to ~5% at 1000 nm.

In terms of timing jitter, there have been reports of thin junction devices having exhibited jitter responses of 20 ps FWHM, although these were in small area diameter devices (~10 μm) [120]. Thick junction devices generally exhibit timing jitter of the order of 520 ps FWHM in a 200 μm diameter active area [121]. It should be noted that some authors have reported much improved timing jitter through adaptations of read-out electronics [121].
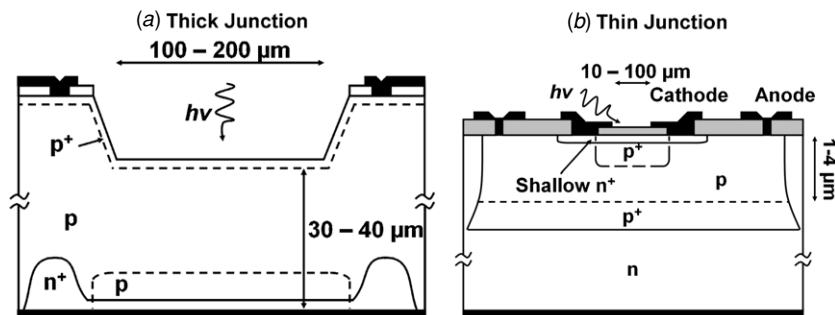
Figure 21. Left: a schematic of a thick junction silicon single-photon avalanche diode (Si-SPAD). Right: a schematic of a thin junction Si-SPAD with [118].
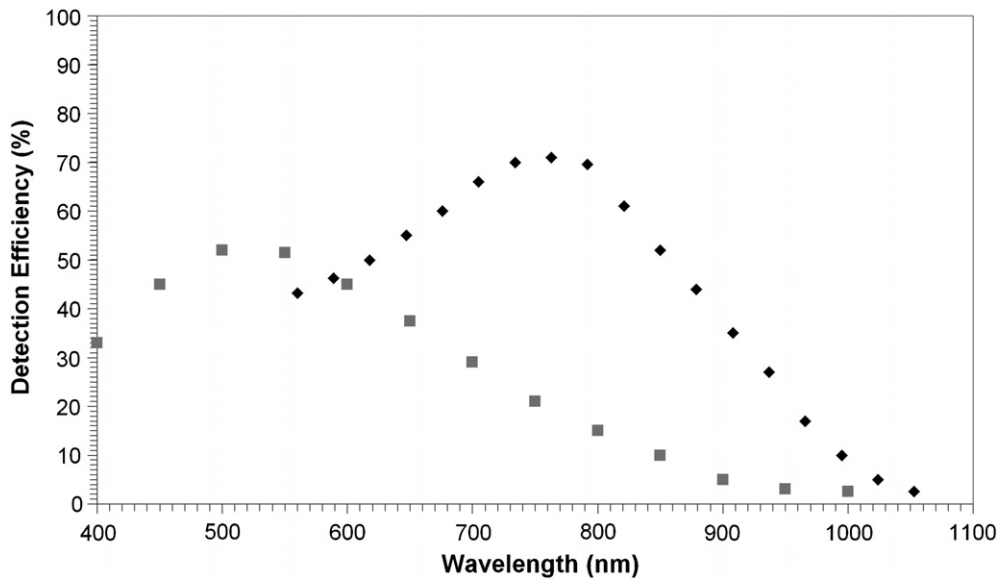
Figure 22. A comparison of the detection efficiencies of thick (diamonds, ◆) and thin junction (squares, ■) silicon single-photon avalanche diodes (Si-SPADs) [109].

The reduction in the thickness of the junction leads to a reduction in the timing jitter but also a reduction in the detection efficiency. Early designs of thin junction SPAD exhibited long diffusion tails [122–124] whereby the instrumental response has a peak followed by a long, exponential tail caused by photogenerated carriers which are generated by absorption in the substrate of the device which then reach the depletion layer by diffusion and generate further avalanches. At $\frac{1}{100}$th of the maximum, the full-width (FW1/100M) of the detector response could be as great as 650 ps for comparatively short FWHM of ∼35 ps [125]. Later version of these devices improved the FW1/100M to 130 ps by reducing the thickness of the neutral layer beneath the active junction [125].

Generally, the dark count rate of a thin junction Si-SPAD depends on the diameter of the active area [125]. Typical values at 20 °C are ∼700 count s^{-1} for 50 μm, diameter ∼3000 count s^{-1} for 100 μm diameter and ∼ 40 000 count s^{-1} for 200 μm diameter [125]. As the device is cooled, the probability of thermally generated carriers falls and the dark count rate falls. At a temperature of −25 °C the dark count rates become 5 count s^{-1}, 50 count s^{-1} and 1500 count s^{-1} respectively [125]. At a wavelength of 850 nm a typical commercial thick junction Si-SPAD at a temperature of ∼ −25 °C will exhibit an NEP of ∼8 × 10^{-18} W Hz$^{-1/2}$ while a 200 μm diameter active area thin junction at the same wavelength and a temperature of −25 °C will exhibit an NEP of ∼7 × 10^{-17} W Hz$^{-1/2}$ [125], and at room temperature the higher NEP of ∼7 × 10^{-16} W Hz$^{-1/2}$. However, it should be noted that reduced NEP is readily observed with smaller diameter devices, for example an NEP of 1.5 × 10^{-17} W Hz$^{-1/2}$ was measured using a 50 μm diameter shallow-junction Si-SPAD at −15 °C at a wavelength of 850 nm [126]. At room temperature a 50 μm diameter shallow junction Si-SPAD has demonstrated an NEP of 4.7 × 10^{-17} W Hz$^{-1/2}$ [127] at a wavelength of 850 nm.

Just as in the case of some single-photon sources, it is possible to use a resonant cavity to increase the efficiency of SPAD detectors [128]. It is possible to form a cavity of this type by using a reflector buried in the device and the air/semiconductor interface at the top [128, 129], leading to a higher detection efficiency for the same depletion region thickness. This can be used with thin junction SPADs to increase the detection efficiency while avoiding an increase in timing jitter [118]. The introduction of a cavity into a thin junction Si-SPAD using silicon-on-insulator (SOI) in the lower mirror was shown by Ghioni *et al* [125] to increase the detection efficiency from 10% to 34% at a wavelength of 850 nm. This prototype device has a high room temperature dark count rate of 100 000 count s^{-1} for a 50 μm diameter active area, due to dislocations induced by the SOI layers by temperature-induced strain relaxation.

As was discussed previously, the main advantage of PMT detectors is the large active area when compared to Si-SPADs. One possible solution is to produce a 'large area' detector which is a series of interconnected Si-SPADs in a grid formation. Each element in the grid (or pixel) is a SPAD. The SPADs are joined together on a common substrate and output across a common load resistor so that the electrical outputs of each pixel are summed [130]. Consequently, it is possible to use these interconnected Si-SPADs in photon number resolving experiments as, provided the photons are incident on different pixels, coincident photon events will generate an electrical output pulse which is correspondingly higher by a factor depending on the number of pixels which were illuminated. All of the electrical outputs from the individual pixels are combined, adding dark count contributions from each pixel to the total dark count rate. A typical fill factor for a 1 mm^2 SiPM is about 25% [130].

The single-photon detection efficiencies of interconnected Si-SPADs are, as would be expected, similar to those of single silicon SPADs. An example interconnected Si-SPAD matrix,
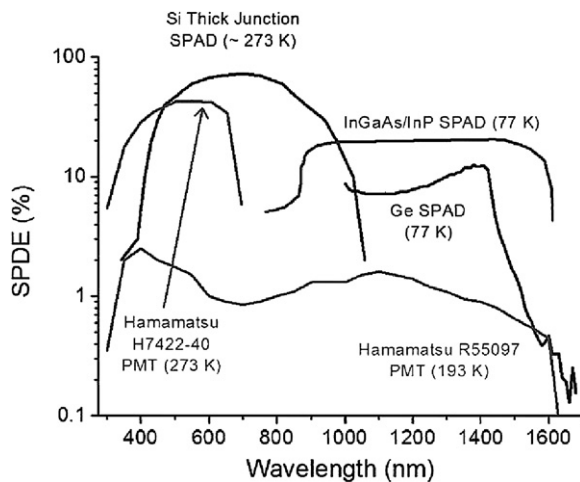
Figure 23. Plot of single-photon detection efficiencies versus wavelength for a silicon thick junction single-photon avalanche diode (SPAD), an InGaAs/InP avalanche photodiode (APD) operated in Geiger mode, a germanium SPAD, a Hamamatsu Infrared Photomultiplier Tube (PMT), and a visible wavelength high-efficiency Hamamatsu PMT.

such as that developed by SensL in 2008, has a single-photon detection efficiency of the order of 20% at a wavelength of 500 nm, decreasing to approximately 6% at 800 nm [131, 132]. The NEP of a 1 mm^2 SensL detector with 620 elements is $\sim 9 \times 10^{-15}$ W Hz$^{-1/2}$ at a temperature of $-4\,^{\circ}$C [133].

Recent advances in arrayed silicon SPADs [134–136] also provide possible options as highly sensitive focal plane arrays, and, in some cases, these arrays permit individual timing information from each pixel. Arrayed Si-SPADs consist of a 2D matrix of independently electrically addressed SPAD detectors covering a large area, typically several mm^2. The addressing and read-out electronics tend to take a high proportion of the area between pixels, leading to low fill factors. Arrayed silicon SPADs have found applications in fields such as 3D imaging [135] and astronomy [134] where they have the potential to reduce measurement durations. Niclass *et al* used a 32 × 32 array of SPADs to demonstrate a 3D imager based on time-of-flight [135], with each pixel exhibiting 115 ps timing jitter (FWHM). A separate depth measurement was performed for each pixel in the array and the 1024 independent measurements combined to produce a 3D image of the target. The NEP of a typical pixel was $\sim 6 \times 10^{-17}$ W Hz$^{-1/2}$ at a temperature of 0 $^{\circ}$C. Zappa *et al* presented a 60 pixel array for use in astronomical applications where the photon numbers involved in measurements can be extremely low but there is a desire to undertake measurements for only a short time period due to the rapid nature of the phenomena under examination [134]. The maximum saturated count rate of this detector was 30 Mcount s^{-1} while the minimum was at the single-photon level. The NEP of a single pixel in this array was $\sim 3 \times 10^{-17}$ W Hz$^{-1/2}$ at a temperature of $-10\,^{\circ}$C.

3.4.3. Germanium single-photon avalanche diodes. In the mid-1990s, commercially available linear multiplication germanium APDs were characterized in Geiger mode [136, 137], as potential photon-counting detectors in the

infrared. Their quantum efficiency performance compared to that of other SPADs and two PMTs is displayed in figure 23. The main problem with Ge SPADs was the high DCR which was reduced by cryogenic cooling. At room temperature, Ge would absorb at wavelengths beyond 1550 nm, but at the temperatures the devices were tested (77 K), the cut-off was a little under 1500 nm. The SPDE of a Ge SPAD was measured in gated mode to be a modest $\sim 10\%$ and sub-100 ps timing jitter. Ge devices also suffered from a high level of afterpulsing, a phenomenon also apparent in the InGaAs/InP devices which will be discussed later.

3.4.4. Silicon germanium single-photon avalanche diodes. One step towards low-noise linear multiplication APDs was the use of separate absorption and multiplication hetero-structures. Whilst most progress was made in III–V structures, e.g. InGaAs/InP as described below, some progress was made in the use of Ge-containing absorbing layers on Si multiplication layers. The 1980s saw progress towards the development of strained layer silicon/silicon germanium (Si/SiGe) absorbing avalanche diodes grown on Si [138, 139] and used in linear multiplication mode. The devices were fabricated with the absorption in the Si/Si$_{1-x}$Ge$_x$ alloy layers and multiplication in the Si layers. In 2002, the first attempt at a SPAD grown using a similar approach was made by Loudon *et al* [140], where clear improvements in quantum efficiency were found in the near infrared over otherwise identical all-Si control samples. However, such devices used strained SiGe/Si layers with Si/Si$_{0.7}$Ge$_{0.3}$ multiple quantum well material as an absorber, where the thickness of the Ge-containing layer was kept low—a total of only 300 nm including the all-Si layers— in order to keep below the critical thickness of the layer and inhibit relaxation. Such thin layers meant that the overall absorptance in the infrared was low. In later work by Carroll *et al* [141], a 400 nm thick Ge absorber was grown on Si to demonstrate linear multiplication and dark counting above avalanche breakdown.

3.4.5. Indium-phosphide-based single-photon avalanche diodes. Currently, the most promising candidates for near-room temperature single-photon counting at a wavelength of 1550 nm are indium-phosphide (InP)-based separate absorption and multiplication avalanche diodes, particularly InGaAs/InP devices [142, 143]. These devices have been used as linear multiplication devices [144] for many years and have been more recently used above avalanche breakdown, in Geiger mode. In the last few years, specific growth and fabrication programmes aimed at designs for single-photon operation have yielded devices with improved performance [145, 146].

Figure 24 illustrates a schematic of a planar geometry InGaAs/InP SPAD detector, where incident infrared photons are absorbed in the narrow-gap InGaAs and, the photo-generated holes drift to the high-field InP, where multiplication takes place. One potentially important issue in such devices is a large valence band discontinuity in these devices which can result in the delay or recombination of devices at the interface. To combat this, a thin layer (typically 100 nm) of
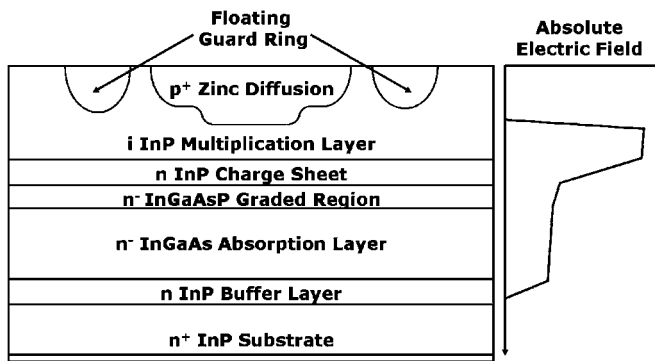
Figure 24. Layer structure of planar geometry InGaAs/InP single-photon avalanche diode. The junction is formed by the diffusion of zinc (Zn) into n-type InP and typically is fabricated with multiple diffusion steps and guard rings in order to avoid preferential edge breakdown.

intermediate gap InGaAsP grading layer is grown between the InP and InGaAs layers to provide a graded step for the drifting photogenerated holes to traverse.

Initially, most work using InGaAs/InP SPADs has used an elementary form of gated quenching operation, typically at low temperatures to counteract the effects of inherently high dark count rates. For example, Hiskett *et al* [143] reported an NEP of 1×10^{-16} W Hz$^{-1/2}$ at 77 K with a Fujitsu linear multiplication device operated in Geiger mode in 1998. By 2001, the same group reported an NEP of 4×10^{-17} W Hz$^{-1/2}$ at the same temperature with an Epitaxx linear multiplication avalanche photodiode. At all temperatures, sub-nanosecond jitter measurements were reported by a number of groups. Aside from the practicality of low temperature operation, serious performance issues also occur as a result of the longer trap lifetimes. Afterpulsing in such a SPAD occurs where an avalanche current fills mid-band gap trap states in the material which then emit carriers at a later time causing further 'dark' (i.e. not directly induced by a photon) events. The resulting higher afterpulsing rates can only be reduced by having a bias below the breakdown threshold after each event, in order that the traps can be emptied without resulting in an avalanche pulse. Consequently, only low gating rates are possible to avoid afterpulsing, where the maximum rate depends on the temperature, the gate duration as well as the constituent material properties, but will generally be prohibitively low, typically in the 1–100 kHz range. Most successful approaches for the reduction of this phenomenon have relied on improved quenching methods to reduce the charge flow per event. Improved quenching approaches, such as very rapid gating at near 1 GHz or greater [147, 148] have been used to reduce the effect of afterpulsing at 223 K temperature operation. Yuan *et al* [149] used a self-differencing circuit to reduce the charge required for the recording of each photon event resulting in reduced afterpulsing and operation at gigahertz clock rates.

These gigahertz gating approaches can work well at near room temperature operation for the application of quantum key distribution where the photon events occur in pre-defined time windows. However, some applications, such as photon-counting time-of-flight ranging [17] or time-resolved luminescence ideally require an ungated detection technique

for more efficient data acquisition. Ungated operation has been realized using rapid active quenching, to permit free-running operation at 210 K [150]. Recent results with low-bias passive quenching have shown room temperature operation with no electrical gating, in a completely free-running mode, although the sensitivity was $\sim 1 \times 10^{-14}$ W Hz$^{-1/2}$ [151]. Greater understanding of the principal dark count mechanisms, eg field-assisted tunnelling in the InP, has led to further improvements in sensitivity via the introduction of longer InP multiplication region [152, 153]. Use of these devices in the low-bias regime have led to room temperature operation with no electrical gating with NEP of $\sim 1 \times 10^{-15}$ W Hz$^{-1/2}$, reducing to 5×10^{-17} W Hz$^{-1/2}$ at 210 K [154], with 10^6 count s per second operation demonstrated.

Other methods of reducing the single-photon induced avalanche pulse have been used where the feedback layers have been incorporated within the device structure. An early example of this uses InGaAs absorber layers and InAlAs multiplication grown on InP [155], and feedback provided by the avalanche pulse altering a hetero-barrier height within the structure, permitting self-quenching and self-recovery.

Despite a number of issues regarding afterpulsing and dark count rates, InP-based SPADs remain the outstanding candidate for practical single-photon detection at 1550 nm wavelength. Although significant improvements have been reported in terms of quenching approach and structure design, the major issue of the origin of afterpulsing phenomenon remains. Although several groups have reported evidence that the traps responsible for afterpulsing are found in the InP layers [156, 157], serious attempts at the removal of the defect complexes have yet to begin. A concentration of research in this area is likely to yield further improvements, leading to reduced dark count rates and higher photon counting rates.

3.5. Hybrid photodetector

It is possible to combine avalanche diodes with photomultiplier tubes to produce hybrid photodetectors (HPDs) [158]. In a hybrid photodetector, an avalanche diode is placed in a vacuum tube with a photocathode at the optical input. Photoelectrons generated at the photocathode are focused onto the smaller area avalanche diode and undergo avalanche gain to produce a detectable current pulse. This technique has the advantage over the PMT that there is a lower spread of transit times for the electrons and, hence, a lower timing jitter [159]. These detectors exhibit good sensitivity, and would be particularly suitable for applications requiring a large detection area.

In 2009 Zhang *et al* employed an up-conversion assisted (see later) hybrid photodetector to QKD [160]. The NEP of the HPD alone was $\sim 5.9 \times 10^{-17}$ W Hz$^{-1/2}$ when illuminated with photons with a wavelength of 600 nm. The FWHM timing jitter of the combined up-conversion and hybrid photodetector was ~ 70 ps at a photon count rate of 200 kcount s^{-1}, rising to ~ 120 ps at 10 Mcount s^{-1} when measured with a 10 ps input pulse. The FW1/10M were ~ 130 ps and ~ 190 ps respectively. The addition of the periodically-poled lithium niobate waveguide used for up-conversion increased the dark count rate and reduced the overall quantum efficiency so
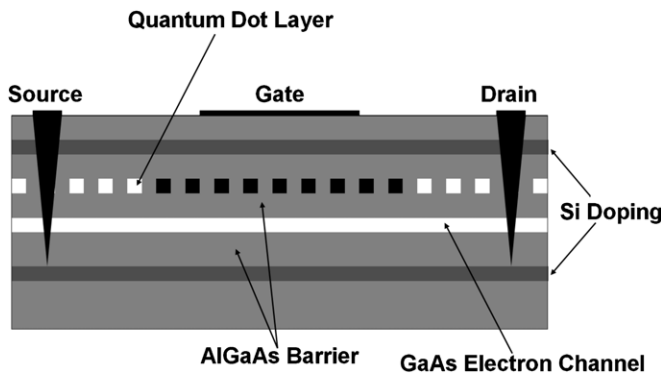
Figure 25. Schematic of the cross section of the quantum dot (QD) single-photon detector. Different layers grown by molecular beam epitaxy (MBE) are represented by varying shades of grey and 'active' dots in the device are shown in black [163].

Figure 26. Quantum dot optically gated field-effect transistor as a single-photon detector [164].

Figure 27. Schematic band structure of a quantum dot resonant tunnelling diode in forward bias (black solid lines) and after capture of photo-excited hole (grey dotted lines) [165].

that the NEP of the combined up-conversion and hybrid photodetector system was $\sim 7.8 \times 10^{-16}$ W Hz$^{-1/2}$. This system operated with a clock frequency of 2 GHz and was able to generate secure key at a rate of 1.3 MBit s^{-1} over 10 km of dispersion-shifted optical fibre.

3.6. Quantum dot-based detectors

As we have already seen in a previous section, it is possible to use the nanometre scale semiconductor structures known as quantum dots to generate single photons. It is also possible to use quantum dots to detect single photons. A field effect transistor (FET) uses an electric field to control the shape, and hence the conductivity, of a channel of one type of charge carrier in a semiconductor material. Following on from the work of Shields *et al* [161], in 2002, Kardynal *et al* [162] demonstrated a quantum dot FET which was capable of single-photon detection—a schematic of which is shown in figure 25. This particular device was based around a GaAs/Al$_{0.33}$Ga$_{0.67}$ As FET with the gating provided by the layer of quantum dots. A single-photon incident on the device generates a photo-electron which is subsequently captured by a quantum dot. This capture changes the shape of the electric field in the FET and produces a measurable change in the source-drain current of the FET.

When cooled to an operating temperature of 77 K this device demonstrated a single-photon detection efficiency of approximately 0.9% for photons at a wavelength of 650 nm, resulting in an NEP of approximately 2×10^{-16} W Hz$^{-1/2}$. It was suggested that the operational wavelength could be shifted to the low loss optical fibre window wavelength of 1550 nm by translating the layer structure to InGaAs/InAlAs although, to the best of the authors' knowledge, this has not yet been demonstrated. In 2007, the same group demonstrated photon number resolving capability using the same structure of quantum dot FET [163] and in 2006, Rowe *et al* reported an internal quantum efficiency of up to $68 \pm 18\%$ at 800 nm operating at 4 K with the device shown in figure 26, which used a GaAs/Al$_{0.20}$Ga$_{0.80}$ As FET [164]. The overall SPDE of this device was limited to between 2% and 3% by the
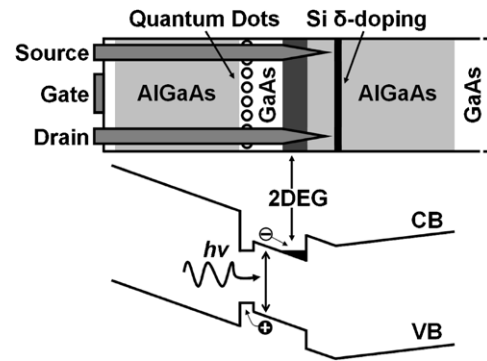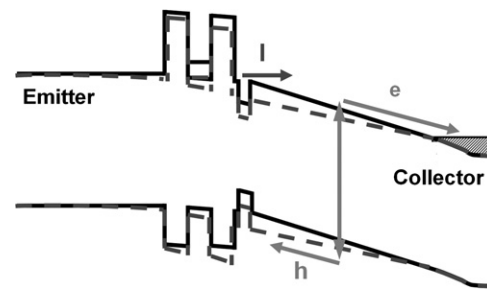
transmission of the semitransparent Pt Schottky barrier gate and the absorption in the active GaAs layer.

In 2007, Blakesley *et al* demonstrated the quantum dot resonant tunnelling diode [165]. In figure 27, the black solid lines show the band structure of the device under forward bias, close to resonance. A sharp resonance is observed in the tunnel current at voltages where the energy of the electrons behind the emitter side barrier is aligned with a confined level in the quantum well between the barriers. Under these conditions, the electrons trapped within the quantum dot induce a potential which affects the tunnelling characteristics. The current flowing between the emitter and collector is restricted by tunnelling through the double barrier. After a photo-excited hole is generated, it is captured by a quantum dot lowering the potential of the dot and thereby changing the resonant tunnelling condition, as shown by the grey dashed lines in figure 27, producing a measurable signal. Although the timing jitter of these detectors at an operating temperature of 4 K was 150 ns, the detection efficiency was greatly improved to a maximum of 12.5% with a dark count rate of 2×10^{-3} s^{-1} when illuminated with a laser of 550 nm wavelength [165], leading to an approximate NEP of 2×10^{-19} W Hz$^{-1/2}$. In these devices, dark counts are generated by electrons escaping from a quantum dot. This is one of the reasons that the devices are operated at such low temperatures—it is highly improbable that an electron escape will be triggered by thermal energy. Consequently, it has been proposed that tunnelling is responsible, dependent on the confinement energy and the electric field over the barrier layer. To increase the

confinement, a material with higher barriers for electron and holes could be used.

For applications such as long distance quantum key distribution it is preferable to have detectors which are capable of operating at wavelengths around 1300 nm or 1550 nm, the low-loss windows of telecommunications fibre [166]. Consequently, in 2007 Li *et al* published details of work on an InP-based AlAs/In$_{0.53}$Ga$_{0.47}$As/AlAs quantum dot resonant tunnelling diode capable of detecting photons with a wavelength of 1.3 μm with a detection efficiency of 0.35% at a certain discriminator level and a temperature of 4.5 K [167]. The authors suggested that this detection efficiency could be increased by using a thicker absorption layer.

3.7. Superconducting detectors

3.7.1. Transition edge sensors. Transition edge sensors offer a means of detecting photons which is based on superconductivity [168]. A superconductor is a material which can support an electrical current without a voltage drop. Superconductivity was first observed in 1911 in mercury by Dutch physicist Heike Kamerlingh Onnes and his assistant Gilles Host. Host discovered that cooling mercury to below 4.2 K (the transition temperature, T_C, above which superconductivity ceases [27]) causes the dc resistivity to fall from 0.12 Ω at 4.225 K to 10^{-5} Ω at 4.19 K [169]—a discovery for which Onnes received the Nobel Prize in Physics in 1913 [170]. Following this discovery, in 1913 it was found that lead (Pb) superconducts at 7.2 K and niobium (Nb) at 9.2 K, the highest transition temperature of all elemental metals [170, 171].

Work progressed throughout the twentieth century and into the early years of the 21st century on research into further superconducting materials and potential applications. One field of research has focused on potential uses for superconductors and is from this work that the transition edge sensor has been developed. Transition edge sensors are a form of extremely sensitive calorimeter [172, 173], a device which allows the measurement of the heat generated during a physical process, such as a chemical reaction. Ideal materials for use in transition edge sensors, such as tungsten, are characterized by a sharp transition between the temperatures at which they superconduct and the temperatures at which they behave as normal conductors [174].

Typically a calorimeter has an absorber which is designed to increase in temperature, a thermometer and a weak link to a thermal heat sink [175]. The device is cooled below the superconducting transition temperature and a bias voltage is applied to increase the temperature of the absorber above that of the substrate to a point where a small increase in temperature will result in a large transition in the resistance [175]. A photon is absorbed in the absorber producing a photoelectron which heats up the absorber. An increase in the temperature of the absorber results in an increase in the resistance of the device and an increase in resistance leads to increase in temperature [174]. This change in resistance can then be measured by external circuitry to provide the detection of single photons.

In some transition edge sensors, tungsten acts as both absorber and thermometer [175] and is patterned onto silicon substrates [174]. The additional heat caused by photon absorption, which is above that present in normal operation, is removed by negative electrothermal feedback (ETF) operating on the tungsten transition edge sensor—the increase in the tungsten's electron temperature increases the resistance and results in a drop in the Joule power dissipated. Due to the relatively weak coupling between the electron and phonon systems at these temperatures when the electron system of the tungsten heats up, and is cooled by the ETF, very little of the excess heat is lost through thermal conduction to the phonon system and substrate [173]. The change in current caused by the change in resistance is measured with a superconducting quantum-interference device (SQUID) array [176]. These detectors offer excellent single-photon detection efficiency at near infrared wavelengths (88% at 1550 nm [175]) and a very low dark count rate of approximately ten counts per second, leading to an NEP of $\sim 6 \times 10^{-19}$ W Hz$^{-1/2}$. In addition, these detectors are capable of photon number resolving [175]. However, they have poor timing attributes with a 90 ns FWHM timing jitter and a reset time of 4 ns [177]. The operating temperature of around 100 mK necessitates cooling through an adiabatic de-magnetization refrigerator [178]. Tungsten-based transition edge sensors can detect a wide spectrum of wavelengths from at least 480–780 nm [174]. They also have low dark count rates [175].

3.7.2. Niobium-nitride superconducting nanowires. In 1957, researchers at the Johns Hopkins University developed a bolometer based on thick superconducting NbN [179]. A bolometer is a type of detector originally developed in 1878 by Samuel Pierpont Langley and used for measuring the incident energy of photons via thermal effects, and typically used in astronomical measurements [180]. Building on the work of Andrews and Strandberg [181] and von Gutfield *et al* [182] with thin-film superconductors, a thin-film NbN bolometer was developed by Bertin and Rose in 1968 [183]. The leap from bolometer to single-photon detector was made by Gol'tsman *et al* in 1991 when they realized that the resistive hotspot formed by the heating effect on an incident photon could lead to single-photon detection [184].

The operation of a superconducting wire detector is outlined in figure 28. Each superconducting wire is biased close to its critical current with a current I_{bias}. An incident photon locally increases the temperature above the critical temperature necessary for superconductivity, forming a resistive hot spot. As the hot spot develops, it leads to the supercurrent becoming concentrated in the peripheral regions around the hot-spot near the edges of the nanowire. If I_{bias} is close to the critical current (I_c) and the current density in the edges of the stripe exceeds the critical current density a non-superconducting barrier is created across the entire width of the stripe. The resulting voltage signal across the contacts of the device can then be amplified for use with conventional time-correlated single-photon (TCSPC) electronics. As the stripe cools, the electrons lose energy through electron–phonon scattering and the hot spot rapidly shrinks, breaking the barrier and restoring the superconductivity. The entire reset process takes 30 ps [185, 186]—far more rapidly than the reset of a
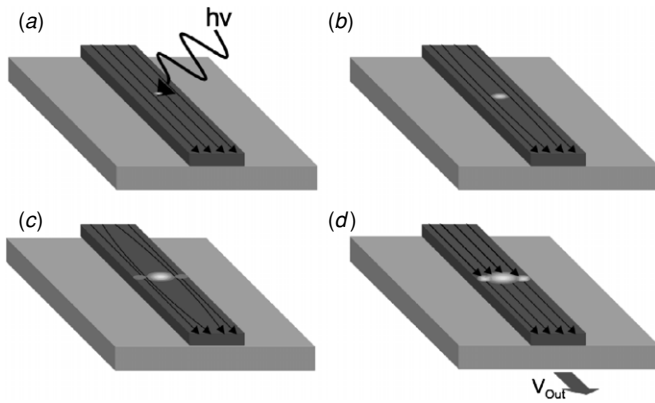
Figure 28. The formation of resistive hot spot in an ultra-thin superconducting stripe, the arrows denote the flow a supercurrent which is biasing the stripe. (*a*) The incident photon suppresses the superconductivity at the hot spot region. (*b*) The small increase in temperature of the hot spot region causes the hot spot to grow as excited electrons propagate away from the initial incident region. (*c*) The hot spot repels the supercurrent, leading it to become concentrated in the regions near the edges of the stripe. (*d*) The current density in these regions exceeds the critical value leading to the formation of a resistive barrier across the width of the stripe. The resulting voltage can then be amplified for use with conventional time correlated single-photon counting (TCSPC) electronics. As the stripe cools, the electrons relax and the hot spot shrinks, breaking the barrier and restoring the superconductivity [186]. After [185].

semiconductor avalanche diode single-photon detector, by any known quenching process.

Early designs suffered from low detection efficiencies as they were based on long, straight wires meaning that the incident photon had to strike the relatively thin 100 nm width of the wire to be detected [185]. The obvious way of increasing the detection efficiency is to increase the area of wire. However, the actual width of the wire cannot be

increased indefinitely due to the small width of the hot spot formed, hence the thin wire was arranged in a meander line as shown in figure 29 [187], in order to present an effective area more consistent with the focusing of visible and infrared light.

The left-hand image in figure 29 shows a typical 100 nm wide superconducting NbN meander wire detector covering a 10 μm × 10 μm area with a fill factor of 50% [187]. Meander type detectors are now available with areas up to 20 μm × 20 μm [188]. These detectors can be coupled to 9 μm core diameter optical fibre with low loss and installed in a Gifford-McMahon type cryogen-free refrigerator systems [178, 189]. A recent version of such a detector system (constructed at Heriot-Watt University, UK) is shown in figure 30, with an operating temperature of 3 K, well below the T_C of 11.5 K.

The process of fabricating an NbN nanowire detector requires several processing steps. First, dc reactive magnetron sputtering in an Ar (argon) and N_2 (molecular nitrogen) environment deposits the NbN film onto the bulk substrate [190]. Next, electron-beam lithography patterns the image of the meander wire onto the surface of the NbN film before a titanium (Ti) mask layer is used with a lift-off process. Finally, the unprotected NbN film is ion milled.

An examination of the effects on detection efficiency of the thickness of the NbN film by Verevkin *et al* [187] indicated that thinner films led to higher detection efficiencies. This is because the diameter of the hot spot generated by an incident photon has an inverse dependency of the thickness so that limitations on the uniformity of the film are eased. A typical thickness is 4 nm [187].

The energy gap in the superconductor is up to three orders of magnitude smaller than in a semiconductor [185] and hence the detector's response extends well into the infrared. Typical detectors have been demonstrated with photons with
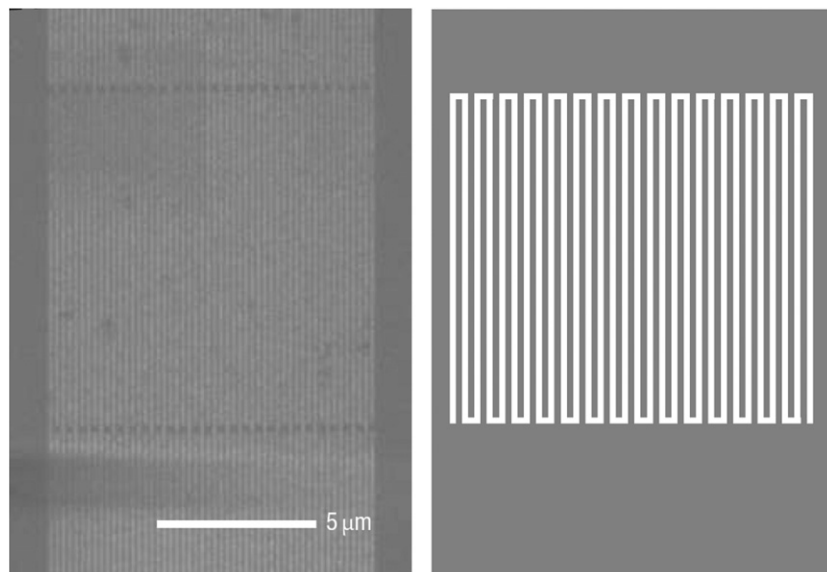
Figure 29. Left: a scanning electron microscope (SEM) image of a superconducting single-photon detector (SSPD). The device consists of a 10 μm × 10 μm meander line with 100 nm wires at a 100 nm pitch [197]. Right: a schematic representation of a smaller detector clearly showing the meander line.
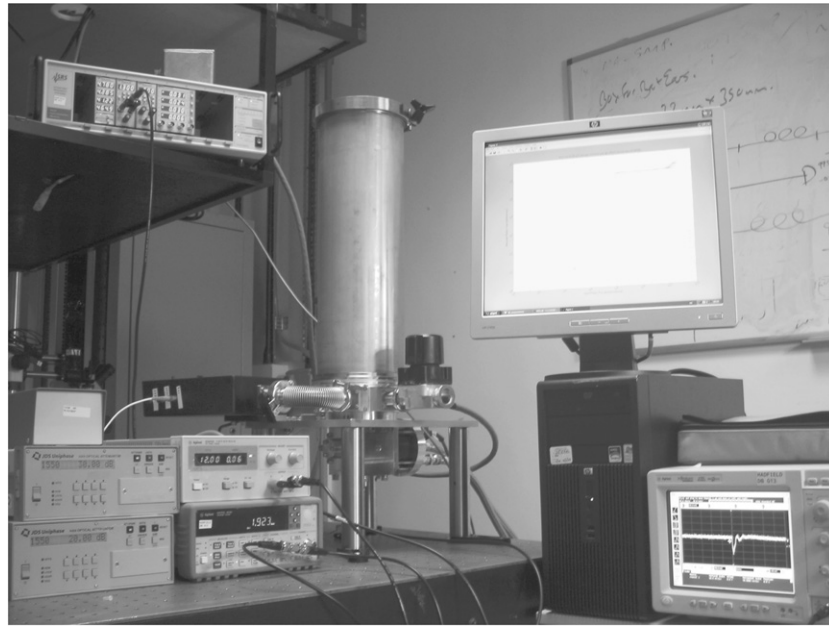
Figure 30. The cylinder near the centre of the picture is the closed cycle refrigerator containing four fibre coupled superconducting single-photon detectors (SSPDs). To the left can be seen the driving electronics and the amplifiers used to produce a signal for use with the standard time correlated single-photon counting (TCSPC) system.

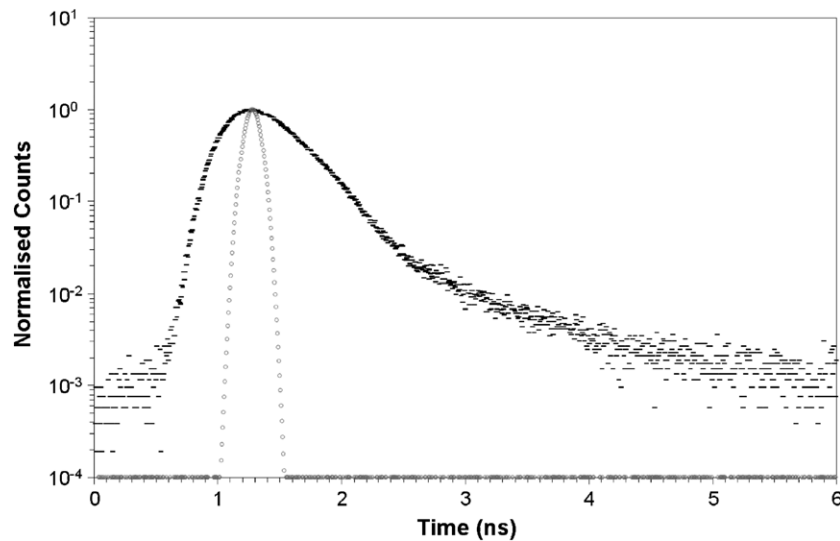**Figure 31.** A comparison between the typical instrumental response functions of an SSPD (grey circles, ○) and a Si-SPAD (black dashes –) taken using a diode laser with a timing jitter of ∼90 ps.

wavelengths from 405 nm to 3 μm [187]. These results demonstrated an NEP of ∼3×10^{-16} W Hz$^{-1/2}$ at a wavelength of 1.55 μm and ∼3×10^{-18} W Hz$^{-1/2}$ at a wavelength of 400 nm.

Superconducting NbN detectors offer low timing jitter with an almost Gaussian temporal profile (68 ps FWHM [191]), fast recovery times (taking less than 10 ns to recover to 90% of the original detection efficiency [192]) and are sensitive to a wide range of wavelengths [193–195]. However, the detection efficiency of these devices is comparatively low [187]. Figure 31 shows a comparison between typical instrumental response functions (IRFs) for the SSPD and a Si-SPAD taken using a diode laser with a timing jitter of ∼90 ps.

The IRF of the Si-SPAD clearly shows a long tail after the initial peak of detection. The dark count rate of the detectors is typically very low at ∼10 counts per second. There is a trade-off between detection efficiency and dark count rate and, typically, the bias current which gives higher detection efficiency will also give a higher dark count rate.

The low timing jitter and dark count rate and wide spectrum of detectable wavelengths of SSPDs makes them interesting candidates for use in many applications. In 2006, Stevens *et al* used an SSPD to examine the lifetime of an infrared emitting quantum well sample optically pumped at 82 MHz with a 1 ps pulse duration mode-locked Ti:sapphire laser at a wavelength of 780 nm [194]. These quantum

wells emitted at wavelengths of 935 nm and 1245 nm where the detection efficiencies of thick junction Si-SPADs are reduced (≈20%), and <0.1% respectively [109]. The lifetimes measured were 150 ps without iterative reconvolution analysis and 58 ps after iterative reconvolution analysis at an emission wavelength of 935 nm and 400 ps and 333 ps respectively at 1245 nm.

SSPDs can also be used for time-of-flight laser ranging. In 2007, Warburton *et al* published work detailing the use of an NbN nanowire SSPD to perform photon-counting time-of-flight ranging at a wavelength of 1550 nm. This wavelength was particularly interesting, where there is a reduced contribution to the overall signal from the solar background [196], improved atmospheric transmission and eye safe operation. In these measurements, the authors resolved a 4 mm surface-to surface separation at a range of 330 metres [93] compared to a previous best result by the same researchers of 1.7 cm using thick junction Si-SPADs with a timing jitter of less than 400 ps [104].

SSPDs have been used for quantum key distribution by Hadfield *et al* [195], Collins *et al* [193] and Takesue *et al* [197]. In 2006, Hadfield *et al* demonstrated a system operated with photons of a wavelength of 1550 nm in a phase-basis-set BB84 protocol. A clock rate of 3.3 MHz was used in conjunction with a quantum channel composed of 42.5 km (equivalent to 8.8 dB loss) to produce a secure key at a net bit-rate of 10 bit s^{-1} and a QBER of 6%. In the same system, an InGaAs SPAD could achieve a secure key at a distance of 25 km (equivalent to 6 dB) at a rate of 8 bit s^{-1} with a QBER of 9.3%.

In 2007, Collins *et al* demonstrated a polarization-basis-set B92 protocol system operating at a wavelength of 850 nm in standard telecommunications fibre, of the type currently deployed in the global telecommunications network [193]. This system was able to transmit secure key over a channel loss of 55 dB (equivalent to 25 km of fibre at this wavelength)—the highest channel loss achieved to that date. Also in 2007, Takesue *et al* demonstrated the highest clock-rate quantum key distribution system at that time, using SSPDs [197]. The master clock operated at 10 GHz and the system used photons with a wavelength of 1557.40 nm in dispersion shifted fibre. These NbN SSPDs had an NEP of 8.1 × 10^{-17} W Hz$^{-1/2}$ at a wavelength of 1557 nm.

One field of research has focused on identifying compounds with higher transition temperatures [171]. At the time of writing, the highest transition temperature is 138 K for a ceramic material composed of mercury, thallium, barium, calcium, strontium, copper and oxygen ($Hg_{1-x}Tl_xBa_2(Ca_{1-y}Sr_y)_2Cu_3O_{8+\delta}$) [198, 199]. The prospect of single-photon detectors based on high temperature superconductors remains distant. It is extremely challenging to grow ultrathin films and fabricate nanostructures in such materials. Any small imperfections in the superconductor will lead to variations in the grain boundaries which limit the upper value of the current density which will, in turn, prevent the formation of the non-superconducting barrier across the stripe which is responsible for the measurable current pulse [185, 199–202]. Also, at a higher operating temperature, the signal-to-noise may be too poor for single-photon detection.

As with SPADs it is possible to use cavities to increase the detection efficiency of SSPDs [203]. The physical design of an SSPD means that it is not possible to form the cavity within the detector and so an external cavity must be formed from a mirror and the surface of the substrate which the detector was grown on [203]. Using this technique it is possible to increase the detection efficiency up to 57% at a wavelength of 1550 nm and 67% at a wavelength of 1064 nm [203].

In 2009, Marsili *et al* demonstrated a parallel array of interconnected superconducting nanowire detectors [204]. As with the grid of interconnected SPADs, this parallel detector array could be used to resolve the number of photons in a pulse if the photons were incident on different detectors. The voltage of the output pulse was dependent on the number of detectors which had registered an event. The number of photons which may be resolved is limited by the number of detectors in the grid.

3.8. Up-conversion

Up-conversion is a technique for the measurement of single photons at longer wavelengths in conjunction with a detector suitable for short wavelengths. For example, this approach has been used to detect single photons of wavelength 1.55 μm using silicon SPADs. This process is the reverse of the parametric down-conversion process described earlier, and is the up-conversion of weak infrared light due to the sum frequency generation under a strong pump or escort beam in a quadratic nonlinear medium. Due to the conservation of energy, the energy of the output photon (expressed as the frequency) must be the sum of both inputs [205, 206], in a similar manner to that expressed in (12). Such an approach has been demonstrated by several authors for the detection of single photons [207–209]. An example is Albota and Wong, with incident photons at a wavelength of 1548 nm where a 980 nm pump beam was used to up-convert to a wavelength of 631 nm and the resulting single photons with this wavelength were detected by a Si-SPAD [208]. By altering the pump power, a range of conversion efficiencies could be achieved, with up to 90% typically being demonstrated. In these experiments, the quasi-phase matched sum frequency generation process was performed in a periodically poled lithium niobate (PPLN) bulk crystal which led to relatively high pump powers of greater than 10 W. The phase matching conditions lead to a relatively small range of spectral bandwidth of ~10.3 nm for the weak beam. Further experiments have utilized other geometries, such a ring lasers [210]. These approaches have yielded high conversion efficiencies, but the dark count rates have been high. Up-conversion has issues of dark counts associated with the escort beam. It is possible for photons from the escort beam to be transmitted through the crystal to the detector or for unconverted photons from the transmission medium to pass through to the detectors [211] These photons can be spectrally separated by use of narrow wavelength bandpass filters although these will also reduce the transmission of photons of the correct wavelength due to physical imperfections [211]. One approach is to increase

Table 1. A summary of example detector parameters from various single-photon detectors.

Detector	Wavelength (nm)	Noise equivalent power (W Hz$^{-1/2}$)	Timing jitter (ps)	Single-photon detection efficiency (%)	Dark count rate (Hz)	Area	Gated	Operating temperature
Si-SPAD (thin junction) [125, 127]	550	1.7×10^{-17}	35	52	300	50 μm (dia.)	No	Room temperature
	850	4.7×10^{-17}		12				
Si-SPAD (thick junction) [116]	830	3.7×10^{-18}	500 (est.)	45	25 (min)	180 μm (dia.)	No	Peltier cooled (253 K min)
InGaAs SPAD [149, 154]	1550	1.5×10^{-15}	500	2.8	40 000	25 μm (dia.)	No	Room temperature
		9.0×10^{-17}	55 (est.)	10.9	2 925	30 μm (dia.)	1.25 GHz	243 K
Tungsten transition edge sensor [175]	1550	6.5×10^{-19}	90 000	88	10	25×25 μm	No	100×10^{-3} K
NbN nanowire [197]	1557	8.1×10^{-17}	60	0.7	$\leqslant 10$	10×10 μm	No	3 K
Hybrid photodetector [160]	600	5.9×10^{-17}	95 (mean)	25	1000	3 mm (photodiode dia.)	Unknown	Room temperature
Up-conversion assisted hybrid photodetector [160]	1550	7.8×10^{-16}	<200	4	30 000		Yes	
Up-conversion [213]	1560	8.0×10^{-16}	50	5	50 000	50 μm (dia.)	No	Room temperature
Quantum dot [165]	550	2.0×10^{-19}	150 000	12.5	2×10^{-3}	1 μm^2 active area	Yes	4 K

[*] Temperature stabilized crystal.

the wavelength of the pump [209], however that necessarily reduces the wavelength of the incident single photons due to energy conservation. PPLN waveguide geometries have been used effectively [211] and more recently with shallow-junction Si-SPADs [212] for improved jitter single-photon detection. To improve the usable bandwidth of this approach, Thew *et al* [213] used a spectrally tuneable pump laser to increase the spectral range of single-photon detection at wavelengths around 1550 nm.

An example of the up-conversion approach to single-photon detection has been used in an optical fibre-based quantum key distribution at a transmission wavelength of 1550 nm, in order to utilize fast Si-SPAD detectors [211]. This system used a differential phase shift quantum key distribution system at 1 GHz clock frequency. The up-conversion process was used to convert the 1550 nm wavelength light to 713 nm using an escort beam at a wavelength of 1.32 μm. This permitted secure bit rates of 166 bit s^{-1} at a distance of 100 km, which at the time was a record for bit rate at such a range.

3.9. Summary of detectors

Table 1 shows a selection of representative parameter values for various example detectors published in open literature. The field of single-photon detection is characterized by many different approaches to the technologies which can result in variations between the parameters for similar detectors. The values summarized in table 1 have been selected be representative of the appropriate detector technology and are intended to give the reader an understanding of the relative merits of each detector technology.

4. Conclusions

This review has provided a brief overview of the evolution and current status of the two interlinked research areas of single-photon detection and single-photon generation. A brief summary has been given of the main technologies in each area and some notable examples of applications have been highlighted. The field has certainly shown many new advances in recent years, particularly in the development of genuine single-photon generation and in new approaches for infrared single-photon counting. While Si-based avalanche diode detectors and photomultiplier approaches continue to improve the 400–1000 nm wavelength region, the stimulus of applications at longer wavelengths means that there is a strong interest in detector development in the near-infrared. The wavelength region at 1.55 μm remains critical for applications requiring compatibility with the existing telecommunications optical fibre infrastructure, as well as providing a low-loss and low solar background window for free-space optical communication. In terms of near-room temperature operation, InGaAs/InP SPADs remain a strong candidate for single-photon detection operation at this wavelength, although developments with low-temperature superconducting detectors, particularly NbN nanowires, show exciting potential for numerous application areas. The emergence of new application areas is strongly married to many of these new detector and source developments.

References

[1] Einstein A 1905 Über einen die Erzeugung und Verwandlung des Lichtes bettreffenden heuristischen Gesichtspunkt *Ann. Phys., Lpz.* **17** 132–48

[2] Stachel J 1998 *Einstein's Miraculous Year: Five Papers That Changed the Face of Physics* (Princeton, NJ: Princeton University Press)

[3] Glauber R J 1963 Coherent and incoherent states of the radiation field *Phys. Rev.* **131** 2766–88

[4] Heisenberg W 1927 Über den anschaulichen Inhalt der quantentheoretischen Kinematic und Mechanik *Z. Phys.* **43** 172–98

[5] Heisenberg W 1983 *The Physical Content of Quantum Kinematics and Mechanics: 62–84* (Princeton, NJ: Princeton University Press)

[6] Bennett C H and Brassard G 1984 Quantum cryptography: public key distribution and coin tossing *Proc. Int. Conf. on Computers, Systems & Signal Processing (Bangalore, India)* pp 175–9

[7] Geneva is counting on quantum cryptography as it counts its votes *Geneva State Chancellery Press Release* 2007 http://www.idquantique.com/news/files/com_swissquantum_ang.pdf

[8] Hammond A and Citrano A 2004 MagiQ Technologies celebrates five years of progress with demonstration of quantum private network *MagiQ Technologies Press Release*

[9] Taylor G I 1909 Interference fringes with feeble light *Proc. Camb. Phil. Soc.* **15** 114–5

[10] Feynman R P 1965 *The Feynman Lectures on Physics* vol 3 (Reading, MA: Addison-Wesley) pp 1–8

[11] Grangier P, Roger G and Aspect A 1986 Experimental evidence for a photon anticorrelation effect on a beam Splitter: a new light on single-photon interferences *Europhys. Lett.* **1** 173–9

[12] Deutsch D 1985 Quantum theory, the Church–Turing principle and the universal quantum computer *Proc. R. Soc.* A **400** 97–117

[13] Shor P W 1994 Algorithms for quantum computation: discrete logarithms and factoring *IEEE Symp. on Foundations of Computer Science* pp 124–34

[14] Knill E, Laflamme R and Milburn G J 2001 A scheme for efficient quantum computation with linear optics *Nature* **409** 46

[15] Bellis S, Jackson C and König A 2005 Photon counting sensors for medical and biophotonic applications *Laser+Photonik* **5** 34–8

[16] Massa J S, Buller G S and Walker A C 1997 Time–resolved photoluminescence studies of cross–well transport in a biased GaAs/AlGaAs multiple quantum well p–i–n structure *J. Appl. Phys.* **82** 712–7

[17] Massa J S, Wallace A M, Buller G S, Fancey S J and Walker A C 1997 Laser depth measurement based on time–correlated single photon counting *Opt. Lett.* **22** 543–5

[18] Bennett C H, Bessette F, Brassard G, Salvail L and Smolin J 1992 Experimental quantum cryptography *J. Cryptol.* **5** 3–28

[19] Hiskett P A, Rosenberg D, Peterson C G, Hughes R J, Nam S, Lita A E, Miller A J and Nordholt J E 2006 Long-distance quantum key distribution in optical fibre *New J. Phys.* **8** 193

[20] Fernandez V, Collins R J, Gordon K J, Townsend P D and Buller G S 2007 Passive optical network approach to gigahertz-clocked multiuser quantum key distribution *IEEE J. Quantum Electron.* **43** 130–8

[21] Gobby C, Yuan Z L and Shields A J 2004 Quantum key distribution over 122 km of standard telecom fiber *Appl. Phys. Lett.* **84** 3762–4

[22] Hiskett P A, Bonfrate G, Buller G S and Townsend P D 2001 Eighty kilometre transmission experiment using an InGaAs/InP SPAD-based quantum cryptography receiver operating at 1.55 μm *J. Mod. Opt.* **48** 1957–66

[23] Townsend P D, Rarity J G and Tapster P R 1993 Enhanced single photon fringe visibility in a 10 km-long prototype quantum cryptography channel *Electron. Lett.* **29** 1291–3

[24] Upton G and Cook I 2004 *Oxford Dictionary of Statistics* (Oxford: Oxford University Press)

[25] Lütkenhaus N 2000 Security against individual attacks for realistic quantum key distribution *Phys. Rev.* A **61** 052304

[26] Townsend P D 1998 Experimental investigation of the performance limits for first telecommunications-window quantum cryptography systems *IEEE Photonics Technol. Lett.* **10** 1048–50

[27] Rohlf J W 1994 *Modern Physics from α to Z₀* 1st edn (New York: Wiley)

[28] Hecht E 1998 *Optics* 3rd edn (Reading, MA: Addison-Wesley)

[29] Kimble H J and Mandel L 1977 Resonance fluorescence with excitation of finite bandwidth *Phys. Rev.* A **15** 689–99

[30] Pinkse P W H, Fischer T, Maunz P and Rempe G 2000 Trapping an atom with single photons *Nature* **404** 365–8

[31] Hijlkema M, Weber B, Specht H P, Webster S C, Kuhn A and Rempe G 2007 A single-photon server with just one atom *Nat. Phys.* **3** 253–5

[32] Ye J, Vernooy D W and Kimble H J 1999 Trapping of single atoms in cavity QED *Phys. Rev. Lett.* **83** 4987–90

[33] Hu Z and Kimble H J 1994 Observation of a single atom in a magneto-optical trap *Opt. Lett.* **19** 1888–90

[34] Ruschewitz F, Bettermann D, Peng J L and Ertmer W 1996 Statistical investigations on single trapped neutral atoms *Europhys. Lett.* **34** 651–6

[35] Neuhauser W, Hohenstatt M and Toschek P E 1980 Localized visible Ba⁺ mono-ion oscillator *Phys. Rev.* A **22** 1137–40

[36] Yariv A 1997 *Optical Electronics in Modern Communications* 5th edn (New York: Oxford University Press)

[37] Hanbury Brown R and Twiss R Q 1956 Correlation between photons in two coherent beams of light *Nature* **177** 27–9

[38] Darquié B, Jones M P A, Dingjan J, Beugnon J, Bergamini S, Sortais Y, Messin G, Browaeys A and Grangier P 2005 Controlled single-photon emission from a single trapped two-level atom *Science* **309** 454–6

[39] Kaiser W and Bond W L 1959 Nitrogen, a major impurity in common type 1 diamond *Phys. Rev.* **115** 857–63

[40] Brouri R, Beveratos A, Poizat J-P and Grangier P 2000 Photon antibunching in the fluorescence of individual color centers in diamond *Opt. Lett.* **25** 1294–6

[41] Kurtsiefer C, Mayer S, Zarda P and Weinfurter H 2000 Stable solid-state source of single photons *Phys. Rev. Lett.* **85** 290–3

[42] Field J E 1992 *The Properties of Natural and Synthetic Diamond* (New York: Academic)

[43] Zaitsev A M 1998 *Handbook of Industrial Diamonds and Diamond Films* ed M Prelas, G Popovici and L Bigelow (New York: Dekker) pp 227–376

[44] Wang C, Kurtsiefer C, Wienfurter H and Burchard B 2006 Single photon emission from SiV centres in diamond produced by ion implantation *J. Phys. B: At. Mol. Opt. Phys.* **39** 37–41

[45] Wu E, Rabeau J R, Roger G, Treussart F, Zeng H, Grangier P, Prawer S and Roch J-F 2007 Room temperature triggered single-photon source in the near infrared *New J. Phys.* **9** 434

[46] Colpin Y, Swan A, Zvyagin A V and Plakhotnik T 2006 Imaging and sizing of diamond nanoparticles *Opt. Lett.* **31** 625–7

[47] Vavilov V S, Gippius A A, Zaitsev A M, Derjaguin B V, Spitsyn B V and Aleksenko A E 1980 Investigation of the cathodoluminescence of epitaxial diamond films *Sov. Phys. Semicond.* **14** 1078–9 (Tranlated from 1980 *Fiz. Tekh. Poluprovodn.* **14** 1811–4)

[48] Clark C D, Kanda H, Kiflawi I and Sittas G 1995 Silicon defects in diamond *Phys. Rev.* B **51** 16681–8

[49] Gaebel T, Popa I, Gruber A, Domhan M, Jelezko F and Wrachtrup J 2004 Stable single-photon emission in the near infrared *New J. Phys.* **6** 98

[50] Rabeau J R, Chin Y L, Prawer S, Jelezko F, Gaebel T and Wrachtrup J 2005 Fabrication of single nickel-nitrogen defects in diamond by chemical vapor deposition *Appl. Phys. Lett.* **86** 131926

[51] Simpson D A, Ampem-Lassen E, Gibson B C, Trpkovski S, Hossain F M, Huntingdon S T, Greentree A D, Hollenberg L C L and Prawer S 2009 A highly efficient two level diamond based single photon source *Appl. Phys. Lett.* **94** 203107

[52] Beveratos A, Brouri R, Gacoin T, Villing A, Poizat J-P and Grangier P 2002 Single-photon quantum cryptography *Phys. Rev. Lett.* **89** 187901

[53] Tomljenovic-Hanic S, Steel M J, Martijn de Sterke C and Salzman J 2006 Diamond based photonic crystal microcavities *Opt. Express* **14** 3556–62

[54] Kreuzer C, Riedrich-Möller J, Neu E and Beecher C 2008 Design of photonic crystal microcavities in diamond films *Opt. Express* **16** 1632–44

[55] Wang C F, Choi Y-S, Lee J C and Hu E L 2007 Observation of whispering gallery modes in nanocrystaline diamond microdisks *Appl. Phys. Lett.* **90** 081110

[56] Wang C F, Hanson R, Awschalom D D, Hu E L, Feygelson T, Yang J and Butler J E 2007 Fabrication and characterization of two-dimensional photonic crystal microcavities in nanocrystaline diamond *Appl. Phys. Lett.* **91** 201112

[57] Park Y-S, Cook A K and Wang H 2006 Cavity QED with diamond nanocrystals and silica microspheres *Nano Lett.* **6** 2075–9

[58] Barth M, Nüsse N, Löchel B and Benson O 2009 Controlled coupling of a single-diamond nanocrystal to a photonic crystal cavity *Opt. Lett.* **34** 1108–10

[59] Warburton R J 2002 Self-assembled semiconductor quantum dots *Contemp. Phys.* **43** 351–64

[60] Michler P, Imamoglu A, Mason M D, Carson P J, Strouse G F and Buratto S K 2000 Quantum correlation among photons from a single dot at room temperature *Nature* **406** 968–70

[61] Santori C, Pelton M, Solomon G, Dale Y and Yamamoto Y 2001 Triggered single photons from a quantum dot *Phys. Rev. Lett.* **86** 1502–5

[62] Santori C, Fattal D, Vuckovic J, Solomon G S and Yamamoto Y 2004 Single-photon generation with InAs quantum dots *New J. Phys.* **6** 89

[63] Blakemore J S 1985 *Solid State Physics* 2nd edn (Cambridge: Cambridge University Press)

[64] de Broglie L 1924 Recherches sur la théorie des quanta *Thesis* (Paris)

de Broglie L 1925 *Ann. Phys., Paris* **3** 22 (Reprinted in 1992 *Ann. Found. Louis de Broglie* **17** 22)

[65] Hook J R and Hall H E 2001 *Solid State Physics* 2nd edn (New York: Wiley)

[66] Dingle R, Wiegmann W and Henry C H 1974 Quantum states of confined carriers in very thin Al$_x$Ga$_{1-x}$As-GaAs-Al$_x$Ga$_{1-x}$As heterostructures *Phys. Rev. Lett.* **33** 827–30

[67] Reed M A, Randall J N, Aggarwal R J, Matyi R J, Moore T M and Wetsel A E 1988 Observation of discrete electronic states in a zero-dimensional semiconductor nanostructure *Phys. Rev. Lett.* **60** 535–7

[68] Reed M A 1993 Quantum dots *Sci. Am.* **268** 118–23

[69] Murray C B, Norris D J and Bawendi M G 1993 Synthesis and characterization of nearly monodisperse CdE (E = S, Se, Te) semiconductor nanocrystallites *J. Am. Chem. Soc.* **115** 8706–15

[70] Lee S W, Mao C, Flynn C E and Belcher A M 2002 Ordering of quantum dots using genetically engineered viruses *Science* **296** 892–5

[71] Bandyopadhyayy S *et al* 1996 Electrochemically assembled quasi-periodic quantum dot arrays *Nanotechnology* **7** 360–71

[72] Stranski I N and Krastanow L 1938 Zur theorie der orientierten ausscheidung von ionen-kristallen aufeinander *Sitz. ber., Akad. Wiss. Wien* **146** 797–804

[73] Markov I and Stoyanov S 1987 Mechanisms of epitaxial growth *Contemp. Phys.* **28** 267–320

[74] Walker P M B 1999 *Chambers Dictionary of Science and Technology* (Edinburgh: Chambers Harrap)

[75] Timpson J A *et al* 2007 Single photon sources based upon single quantum dots in semiconductor microcavity pillars *J. Mod. Opt.* **54** 453–65

[76] Drozdowicz-Tomsia K, Goldys E M and Motlan 2004 Effect of growth temperature of the confinement layer on cathodoluminesence properties of GaSb/GaAs quantum dot multilayer structures *2004 Conf. on Optoelectronics and Microelectronic Materials and Devices* pp 5–8

[77] Long F, Gill S P A and Cocks A C F 2001 Effect of surface-energy anisotropy on the kinetics of quantum dot formation *Phys. Rev.* B **64** 121307

[78] Leonard D, Pond K and Petroff P M 1994 Critical layer thickness for self-assembled InAs islands on GaAs *Phys. Rev.* B **50** 11687–92

[79] Kiravittaya S, Heidemeyer H and Schmidt O G 2004 Growth of three-dimensional quantum dot crystals on patterned GaAs (0 0 1) substrates *Physica* E **23** 253–9

[80] Becker W 2005 *Advanced Time-Correlated Single Photon Counting Techniques* (Berlin: Springer)

[81] Molski A 2000 Photon-counting distribution of fluorescence from a blinking molecule *Chem. Phys. Lett.* **324** 301–6

[82] Purcell E M 1946 Spontaneous emission probabilities at radio frequencies *Phys. Rev.* **69** 681

[83] Strauf S, Stoltz N G, Rakher M T, Coldren L A, Petroff P M and Bouwmeester D 2007 High-frequency single-photon source with polarization control *Nat. Photonics* **1** 704–8

[84] Intallura P M, Ward M B, Karimov O Z, Yuan Z L, See P, Shields A J, Atkinson P and Ritchie D A 2007 Quantum key distribution using a triggered quantum dot source emitting near 1.3 μm *Appl. Phys. Lett.* **91** 161103

[85] Farrow T, See P, Bennett A J, Ward M B, Atkinson P, Cooper K, Ellis D J P, Unitt D C, Ritche D A and Shields A J 2008 Single-photon emitting diode based on a quantum dot in a micro-pillar *Nanotechnology* **19** 345401

[86] Bimberg D *et al* 2009 Quantum dots for single and entangled photon emitters *IEEE Photonics J.* **1** 58–68

[87] Hong C K and Mandel L 1986 Experimental realization of a localized one-photon state *Phys. Rev. Lett.* **56** 58–60

[88] Aichele T, Lvovsky A I and Schiller S 2002 Optical mode characterization of single photons prepared by means of conditional measurements on a biphoton state *Eur. Phys. J.* D **18** 237–45

[89] Fasel S, Alibart O, Tanzilli S, Baldi P, Beveratos A, Gisin N and Zbinden H 2004 High quality asynchronous heralded single-photon source at telecom wavelength *New J. Phys.* **6** 163

[90] Castelleto S, Degiovanni I P, Schettini V and Migdall A 2006 Optimizing single-photon-source heralding efficiency and detection efficiency metrology at 1550 nm using periodically poled lithium niobate *Metrologia* **43** S56–60

[91] Soujaeff A, Takeuchi S, Sasaki K, Hasegawa T and Matsui M 2007 Heralded single photon source at 1550 nm from pulsed parametric down conversion *J. Mod. Opt.* **54** 467–71

[92] Zappa F, Lacaita A L, Cova S D and Lovati P 1996 Solid-state single-photon detectors *Opt. Eng.* **35** 938–45

[93] Warburton R E, McCarthy A, Wallace A M, Hernandez-Marin S, Hadfield R H, Nam S W and Buller G S 2007 Subcentimeter depth resolution using a single-photon counting time-of-flight laser ranging system at 1550 nm wavelength *Opt. Lett.* **32** 2266–8

[94] Collins R J, Hadfield R H, Fernandez V, Nam S W and Buller G S 2007 Low timing jitter detector for gigahertz quantum key distribution *Electron. Lett.* **43** 180–2

[95] Foord R, Jones R, Oliver C J and Pike E R 1969 The use of photomultiplier tubes for photon counting *Appl. Opt.* **8** 1975–89

[96] Burle Industries Inc. 1980 *Photomultiplier Handbook*

[97] Morton G A 1968 Photon counting *Appl. Opt.* **7** 1–10

[98] Rodman J P and Smith H J 1963 Tests of photomultipliers for astronomical pulse-counting applications *Appl. Opt.* **2** 181–6

[99] Gower J 1993 *Optical Communications Systems* 2nd edn (Englewood Cliffs, NJ: Prentice Hall)

[100] Wilson J and Hawkes J 1998 *Optoelectronics: An Introduction* 3rd edn (Englewood Cliffs, NJ: Prentice Hall)

[101] 1999 Hamamatsu Photonics, Hamamatsu R5509–72 specification sheet http://sales.hamamatsu.com/assets/pdf/parts_R/R5509-72.pdf

[102] 1990 Hamamatsu Photonics, Photomultiplier tubes catalogue

[103] http://sales.hamamatsu. com/index.php?id = 13195879

[104] Warburton R E, McCarthy A, Wallace A M, Hernandez–Marin S, Cova S D, Lamb R A and Buller G S 2007 Enhanced performance photon-counting time-of-flight sensor *Opt. Express* **15** 423–9

[105] http://sales.hamatsu. com/en/products/electron-tube-division/detectors/photomultiplier-modules/part-h10330–75.php

[106] 2009 Hamamatsu, Hamamatsu F9892–21/-22 MCP assembly datasheet

[107] Becker W and Bergmann A 2002 *Detectors for High-Speed Photon Counting* (Berlin: Becker and Hickl GmbH)

[108] Degnan J J 2002 Photon-counting multikilohertz microlaser altimeters for airborne and spaceborne topographic measurements *J. Geodyn.* **34** 503–49

[109] Cova S, Ghioni M, Lacaita A, Samori C and Zappa F 1996 Avalanche photodiodes and quenching circuits for single-photon detection *Appl. Opt.* **35** 1956–76

[110] Oldham W O, Samuelson R R and Antognetti P 1972 Tiggering phenomena in avalanche diodes *IEEE Trans. Electron Devices* **19** 1056–60

[111] Vincent G, Chantre A and Bois D 1979 Electric field effect on the thermal emission of traps in semiconductor junctions *J. Appl. Phys.* **50** 5484–7

[112] Martin P A, Streetman B G and Kess H 1981
Electric field enhanced emission from non-coulombic
traps in semiconductors *J. Appl. Phys.*
52 7409–15

[113] Brown R G W, Ridley K D and Rarity J G 1986
Characterization of silicon avalanche photodiodes for
photon correlation measurements. 1: Passive quenching
Appl. Opt. **25** 4122–6

[114] Antognetti P, Cova S and Longoni A 1975 A study of the
operation and performances of an avalanche diode as a
single-photon detector *Proc. 2nd ISPRA Nuclear
Electronics Symp. (Stresa, Italy)* pp 453–6

[115] Cova S, Longoni A and Andreoni A 1981 Towards
picosecond resolution with single-photon avalanche
diodes *Rev. Sci. Instrum.* **52** 408–12

[116] SPCM-AQR single photon counting module Perkin Elmer
Datasheet 2005 http://optoelectronics.perkinelmer.com/
content/Datasheets/DTS_SPCMAQRH.pdf

[117] MPD PDM series. Micro Photon Devices Datasheet 2008
http://www.microphotondevices.com/
media/pdf/PDM_v3_3.pdf

[118] Zappa F, Tisa S, Cova S, Maccagnani P, Calia D B, Saletti R,
Roncella R, Bonanno G and Belluso M 2006
Single-photon avalanche diode arrays for fast transients
and adaptive optics *IEEE Trans. Instrum. Meas.*
55 365–74

[119] Dautet H, Deschamps P, Dion B, MacGregor A D,
MacSween D, McIntyre R J, Trottier C and Webb P P
1993 Photon counting techniques with silicon avalanche
phootdiodes *Appl. Opt.* **32** 3894–900

[120] Sciacca E *et al* 2003 Silicon planar technology for
single-photon optical detectors *IEEE Trans. Electron
Devices* **50** 918–25

[121] Rech I, Labanca I, Ghioni M and Cova S 2006 Modified
single photon counting modules for optimal timing
performance *Rev. Sci. Instrum.* **77** 033104

[122] Cova S, Lacaita A, Ghioni M, Ripamonti G and Louis T A
1989 20-ps timing resolution with single-photon avalanche
diodes *Rev. Sci. Instrum.* **60** 1104–10

[123] Lacaita A, Cova S, Ghioni M and Zappa F 1993
Single-photon avalanche diode with ultrafast pulse
response free from slow tails *IEEE Electron Device Lett.*
14 360–2

[124] Lacaita A, Ghioni M and Cova S 1989 Double epitaxy
improves single-photon avalanche diode performance
Electron. Lett. **25** 841–3

[125] Ghioni M, Gulinatti A, Rech I, Zappa F and Cova S 2007
Progress in silicon single-photon avalanche diodes *IEEE J.
Sel. Top. Quantum Electron.* **13** 852–62

[126] Cova S, Ghioin M, Rech I, Gulinatti A, Giudice A
and Maccagnani P 2008 Silicon single photon avalanche
diodes for quantum key distribution *SECOQC Review*
http://www.secoqc.net/downloads/abstracts/
SECOQC-Cova.pdf

[127] Ghioni M, Gulinatti A, Rech I, Maccaganani P and Cova S
2008 Large-area low-jitter silicon single photon avalanche
diodes *Photonics West 2008. Proc. SPIE* vol 6900
p 69001D

[128] Ünlü M S and Strite S 1995 Resonant cavity enhanced
photonic devices *Appl. Phys. Rev.* **78** 607–39

[129] Emsley M K, Dosunmu O and Ünlü M S 2002 Silicon
substrates with buried distributed Bragg reflectors for
resonant cavity-enhanced optoelectronics *IEEE J. Sel. Top.
Quantum Electron.* **8** 948–55

[130] Buzhan P *et al* 2003 Silicon photomultiplier and its possible
applications *Nucl. Instrum. Methods Phys. Res.* A
504 48–52

[131] 2008 Introduction to the silicon photomultiplier *SensL
Technical Note*

[132] 2007 SPM photon detection efficiency *SensL Technical Note*

[133] Chmill V, Caccia M, Cappellini C, Risigo F and Jastrzab M
2008 Silicon photo multipliers characterization: recent
achievements and latest results. Investigation of SiPM for
photon counting applications *Proc. 10th Conf. on
Astroparticle, Particle and Space Physics, Detectors and
Medical Physics Applications* pp 616–23

[134] Zappa F *et al* 2007 Photon counting arrays for astrophysics *J.
Mod. Opt.* **54** 163–89

[135] Niclass C, Rochas A, Besse P-A and Charbon E 2005 Design
and characterization of a CMOS 3-D image sensor based
on single photon avalanche diodes *IEEE J. Solid-State
Circuits* **40** 1847–54

[136] Owens P C M, Rarity J G, Tapster P R, Knight D
and Townsend P D 1994 Photon counting with passive
quenched germanium avalanche *Appl. Opt.* **33** 6895–901

[137] Lacaita A, Francese P A, Zappa F and Cova S 1994
Single-photon detection beyond 1 micrometer:
performance of commercially available germanium
photodiodes *Appl. Opt.* **33** 6902–18

[138] Luryi S, Pearall T P, Tempkin H and Bean J C 1986
Waveguide infrared photodetectors on a silicon chip *IEEE
Electron Device Lett.* **7** 104–7

[139] Lang D V, People R, Bean J C and Sergent A M 1985
Measurement of the bandgap of Ge_xSi_{1-x}/Si strained
layer heterostructures *Appl. Phys. Lett.* **47** 1333–5

[140] Loudon A Y, Hiskett P A, Buller G S, Carline R T and
Rarity J G 2002 Enhancement of the infrared detection
efficiency in Si photon counting avalanche photodiodes
using SiGe absorbing layers *Opt. Lett.* **27** 219–21

[141] Carroll M S, Childs K, Jarecki R, Bauer T and Saiz K 2008
Ge-Si separate absorption and multiplication avalanche
photodiode for Geiger mode single photon detection *Appl.
Phys. Lett.* **93** 183511

[142] Lacaita A, Zappa F and Cova S 1996 Single-photon detection
beyond 1 μm: performance of commercially available
InGaAs/InP detectors *Appl. Opt.* **35** 2986–96

[143] Hiskett P A, Buller G S, Smith J M, Loudon A Y, Gontijo I,
Walker A C, Townsend P D and Robertson M J 2000
Performance and design of InGaAs/InP photodiodes for
single-photon counting at 1.55 μm *Appl. Opt.* **39** 6818–29

[144] Campbell J C, Dentai A G, Holden W S and Kasper B L 1984
High performance avalanche photodiode with separate
absorption grading and multiplication regions *Electron.
Lett.* **20** 596

[145] Pellegrini S, Warburton R E, Tan L J J, Ng J S, Krysa A B,
Groom K, David J P R, Cova S, Robertson M J and Buller
G S 2006 Design and performance of an InGaAs–InP
single-photon avalanche diode detector *IEEE J. Quantum
Electron.* **42** 397

[146] Itzler M A, Ben-Michael R, Hsu C-F, Slomkowski K, Tosi A,
Cova S, Zappa F and Ispasoiu R 2007 Single-photon
avalanche diodes (SPADs) for 1.5 μm photon counting
applications *J. Mod. Opt.* **54** 283

[147] Namekata N, Sasamori S and Inoue S 2006 800 MHz
single-photon detection at 1550 nm using an InGaAs/InP
avalanche photodiode operated with a sine wave gating
Opt. Express **14** 10043

[148] Namekata N, Adachi S and Inoue S 2009 1.5 GHz
single-photon detection at telecommunication wavelengths
using sinusoidally gated InGaAs/InP avalanche
photodiode *Opt. Express* **17** 6275–82

[149] Yuan Z L, Kardynal B E, Sharpe A W and Shields A J 2007
High speed single photon detection in the near infrared
Appl. Phys. Lett. **91** 041114

[150] Thew R T, Stucki D, Gautier J D, Zbinden H and Rochas A
2007 Free-running InGaAs/InP avalanche photodiode
with active quenching for single photon counting at
telecom wavelengths *Appl. Phys. Lett.* **91** 201114

[151] Warburton R E, Itzler M and Buller G S 2009 Free-running, room temperature operation of an InGaAs/InP single-photon avalanche diode *Appl. Phys. Lett.* **94** 071116

[152] Ramirez D A, Hayat M A and Itzler M A 2008 Dependence of the performance of single photon avalanche diodes on the multiplication region width *IEEE J. Quantum Electron.* **44** 1188–95

[153] Itzler M A, Jiang X, Nyman B and Slomkowski K 2009 InP-based negative feedback avalanche diodes *Proc. SPIE* **7222** 72221K

[154] Warburton R E, Itzler M A and Buller G S 2009 Improved free-running InGaAs/InP single photon avalanche diode detectors operating at room temperature *Electron. Lett.* **45** 996–7

[155] Zhao K, You S, Cheng J and Lo Y 2008 Self-quenching and self-recovering InGaAs/InAlAs single photon avalanche detector *Appl. Phys. Lett.* **93** 153504

[156] Buller G S, Warburton R E, Pellegrini S, Ng J S, David J P R, Tan L J J, Krysa A B and Cova S 2007 Single-photon avalanche diode detectors for quantum key distribution *IET Optoelectron.* **1** 249–54

[157] Tosi A, Dalla Mora A, Zappa F and Cova S 2009 Single-photon avalanche diodes for the near-infrared range: detector and circuit issues *J. Mod. Opt.* **56** 299–308

[158] DeSalvo R, Hao W, You Y, Wang Y and Xu C 1992 First results on the hybrid photodiode tube *Nucl. Instrum. Methods Phys. Res.* A **315** 375–84

[159] Fukasawa A, Haba J, Kageyama A, Nakazawa H and Suyama M 2008 High speed HPD for photon counting *IEEE Trans. Nucl. Sci.* **55** 758–62

[160] Zhang Q *et al* 2009 Megabits secure key rate quantum key distribution *New J. Phys.* **11** 045010

[161] Shields A J, O'Sullivan M P, Farrer I, Ritchie D A, Hogg R A, Leadbeater M L, Norman C E and Pepper M 2000 Detection of single photons using a field-effect transistor gated by a layer of quantum dots *Appl. Phys. Lett.* **76** 3673–5

[162] Kardynal B E, Shields A J, O' Sullivan M P, Beattie N S, Farrer I, Ritchie D A and Cooper K 2002 Detection of single photons using a field effect transistor with a layer of quantum dots *Meas. Sci. Technol.* **13** 1721–6

[163] Kardynal B E, Hees S S, Shields A J, Nicoll C, Farrer I and Ritchie D A 2007 Photon number resolving detector based on a quantum dot field effect transistor *Appl. Phys. Lett.* **90** 181114

[164] Rowe M A, Gansen E J, Greene M, Hadfield R H, Harvey T E, Su M Y, Nam S W, Mirin R P and Rosenberg D 2006 Single-photon detection using a quantum dot optically gated field-effect transistor with high internal quantum efficiency *Appl. Phys. Lett.* **89** 253505

[165] Blakesley J C, See P, Shields A J, Kardynal B E, Atkinson P, Farrer I and Ritchie D A 2005 Efficient single photon detection by quantum dot resonant tunnelling diodes *Phys. Rev. Lett.* **94** 067401

[166] Corning, Corning® SMF-28e® optical fiber product information (PI1344) 2007
http://www.corning.com/assets/0/433/573/583/09573389-147D-4CBC-B55F-18C817D5F800.pdf

[167] Li H W, Kardynał B E, See P, Shields A J, Simmonds P, Beere H E and Ritchie D A 2007 Quantum dot resonant tunnelling diode for telecommunication wavelength single photon detection *Appl. Phys. Lett.* **91** 073516

[168] Perryman M A C, Fodden C L and Peacock A 1993 Optical photon counting using superconducting tunnel junctions *Nucl. Instrum. Methods Phys. Res.* A **325** 319–25

[169] Onnes H K 1911 Further experiments with liquid helium. C. On the change of electrical resistance of pure metals at very low temperatures etc. IV. The resistance of pure mercury at helium temperatures *Commum. Univ. Leiden* vol 120 B

[170] Onnes H K 1913 Investigations into the properties of substances at low temperatures which have led, amongst other things, to the preparation of liquid helium *Nobel Lecture*

[171] Waldram J R 1996 *Superconductivity in Metals and Cuprates* (London: Taylor & Francis)

[172] Irwin K D 1995 An application of electrothermal feedback for high resolution cryogenic particle detection *Appl. Phys. Lett.* **66** 1998–2000

[173] Irwin K D, Nam S W, Cabrera B, Chugg B and Young B A 1995 A quasi-particle-trap-assisted transition edge sensor for phonon-mediated particle detection *Rev. Sci. Instrum.* **66** 5322–6

[174] Cabrera B, Clarke R M, Colling P, Miller A J, Nam S and Romani R W 1998 Detection of single infrared, optical, and ultraviolet photons using superconducting transition edge sensors *Appl. Phys. Lett.* **73** 735–7

[175] Rosenberg D, Lita A E, Miller A J and Nam S W 2005 Noise-free high-efficiency photon-number-resolving detectors *Phys. Rev.* A **71** 061803

[176] Huber M E, Neil P A, Benson R G, Burns D A, Corey A M, Flynn C S, Kitaygorodskaya Y, Massihzadeh O, Martinis J M and Hilton G C 1993 Dc squid series array amplifiers with 120 MHz bandwidth *IEEE Trans. Appl. Supercond.* **11** 1251–6

[177] Hiskett P A, Rosenberg D, Peterson C G, Hughes R J, Nam S, Lita A E, Miller A J and Nordholt J E 2006 Long-distance quantum key distribution in optical fibre *New J. Phys.* **8** 193

[178] Radebaugh R 2004 Refrigeration for superconductors *Proc. IEEE* **92** 1719–34

[179] Smith R A, Jones F E and Chasmar R P 1957 *The Detection and Measurement of Infrared Radiation* (Oxford: Oxford University Press)

[180] Langley S P and Abbot C G 1900 *Annals of the Astrophysical Observatory of the Smithsonian Institution* vol 1 (Washington, DC: US Government Printing Office)

[181] Andrews J M Jr and Strandberg M W P 1966 Thermal microwave phonons *Proc. IEEE* **54** 523–8

[182] Von Gutfeld R J, Nethercit A H Jr and Armstrong J A 1966 Transport of heat from metals to insulators at low temperatures *Phys. Rev.* **142** 436–41

[183] Bertin C L and Rose K 1968 Radiant-energy detection by superconducting films *J. Appl. Phys.* **39** 2561–8

[184] Gol'tsman G N, Semenov A D, Gousev Y P, Zorin M A, Gogidze E M, Gershenzon E M, Lang P T, Knott W J and Renk K F 1991 Sensitive picosecond NbN detectors for radiation from millimeter wavelengths to visible light *Supercond. Sci. Technol.* **4** 453–6

[185] Gol'tsman G N, Okunev O, Chulkova G, Lipatov A, Semenov A, Smirnov K, Voronov B, Dzardanov A, Williams C and Sobolewski R 2001 Picosecond superconducting single-photon optical detector *Appl. Phys. Lett.* **79** 705–7

[186] Kadin A M and Johnson M W 1996 Nonequilibrium photon-induced hotspot: A new mechanism for photodetection in ultrathin metallic films *Appl. Phys. Lett.* **69** 3938–40

[187] Verevkin A, Zhang J, Sobolewski R, Lipatov A, Okunev O, Chulkova G, Korneev A, Smirnov K, Gol'tsman G N and Semenov A 2002 Detection efficiency of large-active area NbN single-photon superconducting detectors in the ultraviolet to near-infrared range *Appl. Phys. Lett.* **80** 4687–9

[188] Miki S, Fujiwara M, Sasaki M, Baek B, Miller A J, Hadfield R H, Nam S W and Wang Z 2008 Large sensitive-area single-photon detectors fabricated on single crystal MgO substrates *Appl. Phys. Lett.* **92** 061116

[189] Hadfield R H, Stevens M J, Gruber S G and Miller A J 2005 Single photon source characterization with a superconducting single photon detector *Opt. Express* **13** 10846–53

[190] Yagubov P *et al* 1996 Quasioptical phonon-cooled NbN hot-electron bolometer mixer at THz frequencies *Proc. 7th Int. Symp. on Space Terahertz Technology (Charolottesville, VA, USA)* pp 303–17

[191] Stevens M J, Hadfield R H, Schwall R E and Gupta J A 2006 Fast lifetime measurements of infrared emitters using a low jitter superconducting single photon detector *Appl. Phys. Lett.* **89** 031109

[192] Kerman A J, Dauler E A, Keicher W E, Yang J K W, Berggren K K, Gol'tsman G and Voronov B 2006 Kinetic-inductance-limited reset time of superconducting nanowire photon counters *Appl. Phys. Lett.* **88** 111116

[193] Collins R J, Hadfield R H, Fernandez V, Nam S W and Buller G S 2007 Low timing jitter detector for gigahertz quantum key distribution *Electron. Lett.* **43** 180–2

[194] Stevens M J, Hadfield R H, Schwall R E, Nam S W, Mirin R P and Gupta J A 2006 Fast lifetime measurements of infrared emitters using a low-jitter superconducting single-photon detector *Appl. Phys. Lett.* **89** 031109

[195] Hadfield R H, Habit J L, Schlafer J, Schwall R E and Nam S W 2006 Quantum key distribution at 1550 nm with twin superconducting single-photon detectors *Appl. Phys. Lett.* **89** 241129

[196] Willebrand H and Ghuman B 2001 *Free Space Optics: Enabling Optical Connectivity in Today's Networks* (Indianapolis, IN: Sams)

[197] Takesue H, Nam S W, Zhang Q, Hadfield R H, Honjo T, Tamaki K and Yamamoto Y 2007 Quantum key distribution over a 40-dB channel loss using superconducting single photon detectors *Nat. Photonics* **1** 343–8

[198] Hur Y H, Park Y K and Park J C 1996 Mercury-thallium-barium-calcium-strontium-copper-oxide 1223 superconductor and method of making same *US Patent* No 5,492,885

[199] 2007 *Mineral Commodity Summaries 2007* (USA: Geological Survey)

[200] Morachkine A 2004 *Room Temperature Superconductivity* (Cambridge: Cambridge International Science Publishing)

[201] Hilgenkamp H and Manhart J 1998 Superconducting and normal-state properties of $YBa_2Cu_3O_{7-\delta}$-bicrystal grain boundary junctions in thin films *Appl. Phys. Lett.* **73** 265–7

[202] Steenbeck K, Eick T, Kirsch K, Schmidt H G and Steinbeiß E S 1998 Tunnelling-like magnetoresistance in bicrystal $La_{0.8}Sr_{0.2}MnO_{3-\delta}$ thin films *Appl. Phys. Lett.* **73** 2506–8

[203] Rosfjord K M, Yang J K W, Dauler E A, Kerman A J, Anant V, Voronov B M, Gol'tsman G N and Berggren K K 2006 Nanowire single-photon detector with an integrated optical cavity and anti-reflection coating *Opt. Express* **14** 527–34

[204] Marsili F, Bitauld D, Gaggero A, Jahanmirinejad S, Leoni R, Mattioli F and Fiore A 2009 Physics and application of photon number resolving detectors based on superconducting parallel nanowires *New J. Phys.* **11** 045022

[205] Armstrong J A, Bloembergen N, Ducuing J and Pershan P S 1962 Interactions between lightwaves in a nonlinear dielectric *Phys. Rev.* **127** 1918–39

[206] Watson E A and Morris G M 1990 Comparison of infrared upconversion methods for photon limited imaging *J. Appl. Phys.* **67** 6075–84

[207] Langrock C, Diamanti E, Roussev R V, Yamamoto Y, Fejer M M and Takesue H 2005 Highly efficient single-photon detection at communication wavelengths by use of upconversion in reverse-proton exchanged periodically poled $LiNbO_3$ waveguides *Opt. Lett.* **30** 1725–7

[208] Albota M A and Wong F N C 2004 Efficient single-photon counting at 1.55 μm by means of frequency upconversion *Opt. Lett.* **29** 1449–51

[209] Dong H, Pan H, Li Y, Wu E and Zeng H 2008 Efficient single-photon frequency upconversion at 1.06 μm with ultralow background counts *Appl. Phys. Lett.* **93** 071101

[210] Pan H, Dong H, Zeng H and Lu W 2006 Efficient single-photon countiung at 1.55 μm by intracavity frequency upconversion in a unidirectional ring laser *Appl. Phys. Lett.* **89** 191108

[211] Diamanti E, Takesue H, Langrock C, Fejer M M and Yamamoto Y 2006 100 km differential phase shift quantum key distribution experiment with low jitter up-conversion detectors *Opt. Lett.* **31** 727–9

[212] Thew R T, Tanzilli S, Krainer L, Zeller S C, Rochas A, Rech I, Cova S, Zbinden H and Gisin N 2006 Low jitter up-conversion for telecom waveelngth GHz QKD *New J. Phys.* **8** 32

[213] Thew R T, Zbinden H and Gisin N 2008 Tunable upconversion detector *Appl. Phys. Lett.* **93** 071104